This is a preprint, the final version is subject to change, of the American Mineralogist (MSA)
Cite as Authors (Year) Title. American Mineralogist, in press.
DOI: http://dx.doi.org/10.2138/am-2018-6151

Revision 2

Petrology of 'Mt. Shasta' High-magnesian Andesite (HMA): A product of multi-stage crustal assembly

Martin J. Streck[1] and William P. Leeman[2, 3]

[1] Department of Geology, Portland State University, Portland, OR 97207
[2] Department of Earth Science, Rice University, Houston, TX 77001
[3] Current address: 642 Cumbre Vista, Santa Fe, NM 87501

ABSTRACT

Occurrences of high-Mg andesite (HMA) in modern volcanic arcs raise the possibility that significant volumes of continental crust could be directly derived from the Earth's mantle. Such rocks are commonly associated with subduction of young, warm oceanic lithosphere or occur in areas heated by mantle convection. A relatively rare occurrence near Mt. Shasta in the Cascades volcanic arc, has been considered to represent one such primary mantle-derived magma type, from which more evolved andesitic and dacitic magmas are derived. Recognition that the Shasta area HMA is actually a hybrid mixed magma, calls into question this notion as well as the criteria upon which it is based. We report new chemical and mineralogical data for samples of the Shasta HMA that bear on the components and processes involved in its formation. Several generations of pyroxenes and olivines are present along with different generations of oxide minerals and melt inclusions. The most magnesian olivines (Fo_{93}) exhibit disequilibria textures, exotic melt inclusions, and reaction rims of Fo_{87} composition; these crystals along with spongy, ~Mg# 87 orthopyroxene crystals are interpreted to be xenocrystic and do not signify a primitive mantle derivation. The groundmass is andesitic with moderate MgO content, and melt inclusions of similar compositions are

hosted by equilibrium olivine (~Fo_{87}). The bulk magma (whole rock) is more magnesian, but primarily due to incorporation of mafic minerals and ultramafic xenolith debris. We propose that the exotic crystal and lithic debris in these rocks is derived from [1] dacitic magmas of possible crustal derivation, [2] prograded ultramafic rocks in the underlying crust, and [3] random lithic debris and crystals derived from conduit wall rocks and earlier intruded magmas within the feeder plexus beneath Shasta. The HMA is inferred to represent a mixture between evolved dacitic and primitive basaltic magmas as well as incorporation of xenolithic crystal cargo. There is no compelling evidence that HMA is present in large volumes, and it is not considered to be an important parental liquid to more evolved magmas at Shasta.

Keywords: High-Mg andesite, Mt. Shasta, Cascades arc, mineral zoning and populations

INTRODUCTION

This paper presents a detailed description of high-Mg andesites (HMA) associated with Mt. Shasta, a prominent Quaternary composite volcano in the northern California Cascade Range. The interpretation of HMAs is a significant fulcrum in evaluating subduction-related magmatic processes and carries important implications for understanding the formation of continental crust in general. Most estimates of average crustal composition are essentially andesitic, so a fundamental issue regards the extent to which crust-forming materials are directly derived from the mantle. The occurrence of adakitic magmas in many modern volcanic arcs may be considered to suggest that this is possible. However, we present compelling evidence that the Shasta HMA is a product of complex mixing, and question its interpretation as a primitive mantle-derived magma. Proponents that it is a primitive mantle-derived magma argue that [1] the effects of hybridization are insufficient to shift its composition significantly from direct melts of a subduction-modified mantle source, [2] such magmas are reasonable parents to more evolved magmas at Shasta, and [3] they therefore must comprise a significant volume. Conversely, we believe the available data summarized in this paper indicate that [1] the

HMA can reasonably be considered to be a mixture between the more volumetrically dominant basaltic and dacitic magmas produced at Shasta, [2] certain features (e.g., presence of Fo_{93} olivine) assumed to be diagnostic of primitive mantle derivation are artifacts of interaction with ultramafic rocks in the underlying crust, and [3] HMA is not likely to be parental to the more evolved andesites and dacites at Mt. Shasta. A critical question concerns the actual volume of such magma and, based on surface exposures (essentially one local vent occurrence), HMA appears to be a relatively minor product. We would argue that this is the case for most volcanic arcs. Certainly for the Cascades, we favor the view that basaltic magmas are the dominant contribution from the sub-arc mantle, and their injection into the crust promotes melting to produce dacitic or more evolved magmas. Although fractional crystallization is inevitable, many intermediate composition arc magmas likely are products of mixing between local mafic and silicic magmas.

Here, we present detailed petrographic, mineralogical and geochemical data for HMA lavas from a satellite vent on the Whaleback shield volcano. These rocks were previously studied by Anderson (1974), who first described their mineralogy and investigated melt inclusions in the phenocrysts. A series of important papers (Stone et al., 1989; Baker et al., 1994; Müntener et al., 2001; Grove et al., 2002; Bindeman et al., 2005; Le Voyer et al., 2010; Martin et al., 2011; Ruscitto et al., 2011) address aspects of their petrology and geochemistry and/or present results of experimental work bearing on their formation and evolution. Assuming that HMAs are little-modified mantle-derived magmas, Grove and coworkers proposed that they were produced by melting of a mantle wedge previously modified by influx of slab-derived hydrous fluids or melts. In contrast, our work (Streck et al., 2007a, b, c) clearly documents the hybrid nature of the Shasta area HMAs, which brings into question their interpretation as primitive magmas and demands reconsideration of previous models constructed on this premise.

Figure 1 presents representative compositional variations in Shasta lavas and serves to illustrate the controversy regarding their petrogenesis. When plotted vs. SiO_2, all major element oxides define approximately linear arrays that collectively differ from trajectories defined by fractional crystallization experiments (Müntener et al., 2001; Grove et al., 2002, 2005). Similar near-linear arrays are seen for other Cascades

volcanoes (e.g., Mt. St. Helens: Smith and Leeman, 1987, 1993; Mt. Lassen: Clynne, 1999; Mt. Baker: Baggerman and DeBari, 2011; Mt. Rainier: Sisson et al., 2014), and all could be produced by mixing between local basaltic and dacitic magmas. Cognate melt inclusions (HMA-type in Fo_{87} equilibrium olivines; "HMA MI" in Fig. 1) and groundmass in the Shasta HMA ("HMA GM" in Fig. 1) plot essentially on the linear arrays, whereas the bulk HMA lava deviates from the array for MgO in a manner consistent with addition of exotic Mg-rich components (Streck et al., 2007c). One such component comprises forsteritic (Fo_{93}) olivines that contain 'primitive basaltic andesite' (PBA-type) melt inclusions that are distinct from all known Shasta lavas and attest to the exotic nature of the host olivines (Ruscitto et al., 2011; cf. our Supplement II in Appendix for more details). Beginning with either local calcalkalic basalt or bulk HMA, the experimentally determined fractionation pathways cannot replicate observed compositions of more evolved lavas. However, experimental partial melts of mafic amphibolites (cf. Gao et al., 2016) indicate that the most evolved (dacitic) magmas could potentially be produced by partial melting of such rocks at deep crustal levels. This raises the possibility that intermediate lava compositions could be produced by mixing between mantle-derived basaltic magmas and melts of preexisting crustal rocks. Here, we further characterize the magmatic and other mixing components identifiable in HMA, and speculate on how these magmas formed in the context of petrogenetic scenarios proposed for the Cascades. Ultimately, this work bears on models for arc magmatism in the Cascades and worldwide.

SAMPLES AND ANALYTICAL METHODS

Field relations

HMA occurrences at Mt. Shasta and surroundings are largely restricted to a scoria cone on the NE flank of the Whaleback shield volcano, located 5 km northeast of Mt. Shasta summit (Figs. 2, 3). All samples of 'Mt. Shasta' HMA investigated by Anderson, Grove and coworkers, and by us were obtained from this location. No other occurrences of HMA have been reported, albeit Barr et al. (2008) mention a lava flow of HMA composition in the vicinity.

Although not directly dated, the age of the HMA scoria cone is estimated to be 160±16 ka (A. Calvert, personal communication). Quarry exposures reveal two tephra sequences separated by a strong angular unconformity (Fig. 3; cf. Anderson, 1974). Layers of the lower sequence are on average thinner (< 30 cm) than those of the upper sequence (0.5 to 2 m). The relative proportions of ash:lapilli:blocks vary, and individual strata range from thin layers comprising mainly coarse ash/fine lapilli, to well sorted layers consisting almost entirely of lapilli, to thicker layers containing abundant blocks and bombs. Samples investigated in this study consist of volcanic ejecta blocks (bombs) and tephra samples, as well as a crosscutting dike (MS-HMA15) that represents the youngest eruptive event discernible in the quarry exposure. Melt inclusions from the two tephra samples (MS-13-04 and MS-14-04) were previously studied by Ruscitto et al. (2011).

Analytical Methods

Whole-rock samples were analyzed for major and trace elements by XRF (Washington State Univ., Geoanalytical Laboratory) and, for selected samples, for ICP-MS trace elements (Rice Univ. and Washington State Univ.), ICP-AES B concentrations (Rice Univ.), and Sr and Pb isotopic compositions (Univ. of Arizona). These data are presented in Table 1. For comparison, we also include in this Table our re-analysis of sample 85-41b along with analyses of the same sample as reported by Grove et al. (2002) and by Magna et al. (2006). LA-ICP-MS analyses were also conducted on representative minerals and groundmass using facilities at ETH (Zurich) and Rice University. All mineral major element analyses were performed using a Cameca SX100 electron microprobe housed at Oregon State University and accessed remotely from Portland State University. Analyses were made using a 30 nA beam current, 15 kV accelerating voltage, and a 1 μm diameter focused beam. Counting times ranged from 10 to 30 sec on peak positions and half these times on background positions. Na was always analyzed first to maximize count rates. Standardization utilized a set of natural materials. Representative mineral analyses are reported for pyroxenes, olivines, oxide minerals, and plagioclase, and trace element analyses of pyroxenes (Supplemental **Tables A1, A2 and A3, A4, A5, respectively**).

LA-ICP-MS data were acquired at ETH using a 193 nm ArF Excimer laser coupled to an ELAN 6100 ICP quadrupole mass spectrometer, and at Rice University using a 213 nm YAG laser coupled to an Element 2 magnetic sector mass spectrometer. Similar laser settings (10 Hz repetition rate) were used in both labs yielding a fluance of about 12 J/cm^2 on the ablation site, with typical beam size of 30 to 60 μm on minerals and 70 μm on groundmass. Trace element contents are reported for selected minerals (Supplemental **Table A5**) and for HMA groundmass (**Table 2**).

Sr and Pb isotopic compositions (**Table 1**) were determined by MC-TIMS and MC-ICPMS, respectively, using methods described by Thibodoux et al. (2007, 2015). $^{87}Sr/^{86}Sr$ ratios are reported with precision better than 0.002% relative to a value of 0.71025 for the NBS-987 reference material. Pb isotopic ratios are reported with external precision better than 0.03% on each ratio based on replicate analyses of NBS-981 reference material with sample ratios normalized to the isotopic composition reported by Galer and Abouchami (1998).

BULK ROCK COMPOSITIONS

Major and trace element compositions are reported for samples that bracket the stratigraphy exposed in the Whaleback quarry. Our analyses compare closely with published data for equivalent samples (Baker et al., 1994; Grove et al., 2002; Magna et al., 2006) as seen by direct comparison for sample 85-41b (**Table 1**). Overall, there is little variation, especially with regard to incompatible elements, and the averaged concentrations for our samples have relative standard deviations smaller than 5-7% for most elements. It is notable that Cr (489-603 ppm) and MgO (7.9-9.1 wt.%) contents systematically increase up section (Fig. 3d). Cr and Ni contents are highest in the dike, which represents the latest eruptive phase that was sampled. There is essentially negligible variation in Pb isotopic composition, whereas the dike has slightly lower $^{87}Sr/^{86}Sr$ than the three earlier ejecta blocks that were analyzed. These subtle changes in composition suggest that the magma reservoir may have been zoned (i.e., toward slightly more mafic bulk composition with depth), or that the eruptions were accompanied by influx of a similar but slightly more mafic magma as eruptions proceeded. To complement this study we also present new analytical data for representative samples of

local basement rocks (e.g., Trinity Ophiolite) and eight other lavas from the Shasta region (cf. Supplemental Table A6).

PETROGRAPHY AND MINERAL COMPOSITIONS

Overview

HMA blocks and lapilli have vesicular textures with 15-20% phenocryst-sized (i.e., >80 μm) crystals and/or aggregates of olivine, clinopyroxene and orthopyroxene as well as smaller groundmass/matrix crystals of these same minerals set in a fine-grained, largely crystalline groundmass. Among phenocryst-sized minerals, orthopyroxene (opx) is most abundant followed by subequal amounts of clinopyroxene (cpx) and olivine, in approximate proportions of 45:30:25, respectively. In the lowermost tephra layers, cpx is clearly more abundant than olivine, but the proportion of olivine increases slightly toward the top of the sequence (as reflected by increasing MgO in bulk rocks; see above). Pyroxene compositions show a large composition range (Fig. 4), but the most remarkable feature of these rocks is their diversity in terms of mineral texture and compositional zoning of individual crystals. Notably, many cpx and opx grains are characterized by conspicuous reverse zoning with Fe-rich cores and Mg-rich overgrowth rims. These minerals are described in detail in the following section, but clearly they signify a complex assembly history for the HMA magma. It should also be noted that xenolithic fragments (up to 0.5 cm) of disaggregated ultramafic material and/or aggregates of olivine ± pyroxene occur in numerous blocks examined (cf. Fig. 3b). Plagioclase is largely confined to the groundmass as microlites, and rare phenocryst-sized grains appear to be in disequilibrium with the host magma. Other minor minerals include Cr-spinel or ilmenite inclusions in ferromagnesian silicates, rare Fe-Cu-Ni sulfide inclusions found predominantly as inclusions in olivines (mainly in micro-xenoliths; cf. Stone et al., 1989), and sparse oxide minerals in the groundmass.

Mineral compositions, zoning and populations

The textures and mineral compositions of Shasta HMA provide critical constraints on the formation of these rocks. Here we provide a detailed description of this remarkable assemblage.

Pyroxenes.

Phenocryst-sized pyroxenes appear to have formed in several different growth environments. Based on distinctive textures, zoning characteristics, and modes of occurrence, we have defined three groups or 'types'. In some cases, these are further subdivided based on subtle variations in these features.

Type 1 pyroxenes include both opx and cpx crystals that exhibit conspicuous step-like reverse zoning with variably thick (<10 to ~50 μm) high-Mg overgrowth rims on lower-Mg interior cores (Fig. 5; cf. Streck, 2008). Overgrowth Mg#s exhibit similar ranges for both cpx (90-86) and opx (93-81), with values predominantly near 87. BSE images of the overgrowths (Fig. 5) reveal no discernible internal discontinuities (e.g., resorption surfaces) and appear consistent with continuous rim growth. The overgrowths typically show a subtle outwardly progressive decrease in Mg# (Fig. 6); thicker growth bands may display step-like decreases (Figs. 5d, 6b). Although opx overgrowth tends to be initially higher in Mg# than cpx overgrowth, data on *Type 3* pyroxenes (see below) clearly attests that both minerals co-crystallized. Overgrowths on both cpx and opx exhibit similar ranges in Cr_2O_3 content (from >1 to ~0.2 wt.%; Fig. 5), and Mg# and Cr contents are generally positively correlated. However, sometimes there is decoupling of Mg# and Cr as exemplified by some grains where maximum Cr content occurs in the middle of the overgrowth band (Fig. 6a; also Fig. 7e of Streck, 2008).

Interiors (cores) of *Type 1* pyroxenes have distinctly higher Fe contents than the rims with Mg# < 80, except as noted below. Where analyzed, zoning in the cores is always normal with Mg# decreasing outward from the interior (Fig. 5b). However, based on differences in composition and zoning characteristics within the cores, we define three sub-types that could signify distinct sources or growth environments for these pyroxenes.

Type 1A pyroxene cores are Fe-rich (Mg# between 59-75 overall) with little zoning (Mg# range < 2%) in any given grain (Figs. 5a, c, d). *Type 1B* crystals have relatively homogeneous but higher Mg# (76-80) cores, but they exhibit a thin (~10 to 50 μm) outer

selvage of slightly more Fe-rich composition (Mg# <76). Included in this group are some larger (>500 μm) crystals with more extremely zoned outer cores (Mg# down to ~70; Fig. 5b). Cores of some *Type 1B* crystals exhibit a growth discordance or hiatus as evidenced by zoning unconformities or even patchy zoning (cf. Streck, 2008). Finally, *Type 1C* crystals are also characterized by distinctly more magnesian cores (Mg# always > 76), but differ from *Type B* grains by the absence of any more Fe-rich compositional domains.

Interfaces between low-Mg# cores and high-Mg# overgrowths in *Type1* pyroxenes are mostly anhedral, albeit subhedral to euhedral forms are sometimes preserved (Fig. 5). On the other hand, the external morphology of *Type 1* crystals is nearly always euhedral due to precipitation of the late overgrowth rims. Some *Type 1* pyroxenes occur as glomerocrystic clusters or aggregates (± inclusions of other minerals); these are more common in the lowermost tephra sequence but are observed throughout the deposit.

Other notable features are as follows. Some *Type 1* grains clearly are fragments of larger crystals that must have been fractured or comminuted shortly before eruption of the HMA magma. This is most evident where low-Mg# portions terminate against the groundmass with straight and angular shapes but with no signs of overgrowth or resorption, whereas other portions of the same crystal do exhibit the high-Mg# overgrowths characteristic of intact *Type 1* pyroxenes (Fig. 5). Also, some *Type 1* pyroxenes contain relicts of distinctive 'patchy zoned' grains (defined below as *Type 2* pyroxenes) that appear to have served as nucleation seeds for Type 1 overgrowths. Rarely, some *Type 1* pyroxenes are strongly resorbed. And finally, the Fe-rich cores of some *Type 1* opx and cpx crystals contain melt inclusions of dacitic bulk composition that are now variably crystallized (Streck et al., 2007a; see below and Table **2**).

Two-pyroxene geothermometry (Putirka, 2008) was applied to subsets of *Type 1* pyroxenes that we interpret to have been essentially coeval. Pyroxene pairs representing high-Mg# (~87) overgrowths give temperatures near 1100°C, that plausibly reflect conditions shortly before the HMA eruption. In contrast, pyroxene pairs representing low-Mg# (~70) cores yield temperatures around 1000°C. The latter are similar to estimates for 1980 Mount St. Helens dacites (~970°C; cf. Smith and Leeman, 1987) and are considered realistic. For comparison, Ruscitto et al. (2011) estimate entrapment

278 temperatures near 1050±35°C for melt inclusions in HMA Fo_{87} phenocrystic olivines; this
279 is consistent with slightly higher temperature for the host magma.
280 *Type 2* pyroxenes (opx only) are distinguished by the presence of distinctive
281 resorption channels (i.e., crystals have pronounced coarse spongy cellular textures)
282 and/or patchy zoning (Fig. 7). The resorption channels have a vermicular appearance
283 under the microscope or in backscattered images (Fig. 7). These channels are either filled
284 with partially crystalline material (indistinguishable from adjacent groundmass) or appear
285 to be empty (Figs. 7a, b, c). Patchy zoning in the remaining orthopyroxene shows great
286 variability in spatial distribution and compositional gradation. These areas appear lightly
287 speckled (at a scale of ~5-20 μm) within a dark matrix (Fig. 7b), although larger patches
288 with complex compositional gradation also occur (Fig. 7c). The morphology and
289 compositional gradients of patchy zoned domains seem inconsistent with simple crystal
290 growth from a single cooling magma, and more likely reflect diffusional or melt reaction
291 processes by which high-Mg opx was replaced by lower-Mg opx – possibly in response
292 to interaction with lower-Mg# melt preceding entrainment of these crystals in the HMA
293 magma.
294 A notable subtype of *Type 2* pyroxene is characterized by distinct overgrowths of
295 very low Mg# (<70) opx that appear to infill cracks and channels (Figs. 7b, d; also Fig.
296 2c of Streck et al., 2007a) and seemingly postdate formation of spongy resorption in the
297 higher-Mg# opx host. For most *Type 2* pyroxenes, the last discernible crystallization
298 'event' is recorded by formation of euhedral, and usually higher-Mg# overgrowths
299 similar to those observed in *Type 1* opx (Figs 7b, c; Fig. 2c of Streck et al., 2007a; Fig. 3b
300 of Streck, 2008). Nevertheless, some *Type 2* crystals do have an anhedral habit and,
301 rarely, they occur as glomerocrystic clusters (Fig. 7d). Finally, small-scale (< ~100 μm)
302 comminuted *Type 2* crystal debris is common in the groundmass.
303 *Type 3* pyroxenes (both cpx and opx) are distinguished by the absence of significant
304 concentric zoning (except for the very outermost few microns of crystals; Figs. 5c, d; 7b).
305 Mg# ranges for cpx (90-83) and opx (93-86) largely overlap. Some *Type 3* pyroxenes
306 display hour-glass zoning that has been attributed to rapid growth, particularly in
307 pyroxene from sub-alkaline magmas (Brophy et al., 1999). They occur predominantly as
308 microphenocrysts (<80 μm) or small phenocrysts (<200 μm), and very seldom as crystals

larger than a few hundred μm. The textural habits of *Type 3* pyroxenes (e.g., intergrowths sharing crystal faces or mutual overgrowths; Fig. 7c) unequivocally suggest simultaneous growth of these pyroxenes coincident with the crystallization of high Mg# overgrowths on *Type 1 & 2* pyroxenes. Some small *Type 3* crystals have skeletal forms that are consistent with rapid growth. Rapid growth and mostly small size of *Type 3* grains suggest crystallization close to eruption and this in turn suggests that variation of Mg# of *Type 3* pyroxene is a function of how the melt composition changed during groundmass crystallization.

In summary, Type 3 opx and cpx appear to have formed directly from the HMA liquid, whereas Types 1 and 2 clearly formed from different liquids and represent antecrystic and/or xenocrystic material.

Olivine

Three distinct olivine populations are recognized based on compositions, textures and crystal sizes. *Type 1* olivines (Fig. 8) appear to be xenocrystic and are rare (± 3 grains per thin section). They generally comprise large (typically > 500 μm, but up to 3 mm) crystals with highly forsteritic compositions (Fo_{92-94}, with most near $Fo_{93-93.6}$). They are mostly anhedral to subhedral in form but exhibit several distinct terminations against the groundmass. In some cases, the anhedral margins are clearly resorbed and show compositional zonation to lower Fo content (Fig. 8d) similar to that of true phenocrysts (~Fo_{87}, see below) in the HMA magma. In other cases, the olivine is overgrown by a reaction selvage of polycrystalline opx that in places also penetrates into the olivine (Fig. 8a). The anhedral margin is sometimes fringed by rapidly crystallized skeletal (~Fo_{87}) olivine (Fig. 8b; cf. Fig. 1 of Streck et al., 2007a) with seemingly little reequilibration of the original olivine. In places, the skeletal fringe grades into a continuous euhedral overgrowth, albeit the anhedral form of the original grain is still evident (Fig. 8c). Lastly, the anhedral margins of some Fo_{93} olivines terminate against groundmass without any preserved selvage (Fig. 8b, top and lower right hand side), consistent with comminution of the xenocrysts near the time of eruption.

Type 2 olivines (Fig. 9) appear to be true phenocrysts of the final HMA magma with maximum size of 400-500 μm in the longest dimension. They commonly have skeletal

forms with spiny to straight edges (Fig. 9a) and feathery shapes. Some are almost completely closed, euhedral grains with triangular inclusions of trapped melt (Fig. 9b). Occasionally, skeletal olivines partially enclose vesicles that predate or were contemporaneous with olivine growth (Fig. 9a). These textures are consistent with rapid growth (cf. Lofgren, 1980; Schiano et al., 2010). The compositions of skeletal olivines are narrowly defined (between Fo_{85-89} with most near Fo_{87}; Fig. 10) and equivalent to olivine microphenocrysts and overgrowths on *Type 1* olivines, and also similar to Mg# of late-formed pyroxenes.

Type 3 olivines occur primarily as multi-grain glomerocrysts with somewhat distinctive compositions (Fo_{88-91}). Varied extinction angles among grains confirm that clusters consist of multiple, interlocking crystals and that these are in fact derived from disaggregated xenoliths (Figs. 9c, 9d). This interpretation is supported by rare observation of undulose extinction within single crystals of olivine. Such glomerocrysts appear to make up the majority of xenolithic olivine debris observed in hand samples (cf. Fig. 3b). Contacts between crystals are often filled by veinlets consisting dominantly of opx, but with abundant spinel and rare plagioclase (Figs. 9c, 9d, 11b). Rare individual olivine crystals having anhedral form and similar compositions are assumed to have the same derivation. NiO contents in the olivines vary from ca. 0.15-0.4 wt.%, and correlate loosely with Fo content (Fig. 10). *Type 2* phenocrystic olivines form a distinct group from the others, whereas there is considerable overlap between *Types 1* and *3*.

Oxides

Oxide minerals are quite rare in samples of HMA. They occur as sparse inclusions in pyroxene and olivine, and are most abundant in opx-dominated veinlets within *Type 3* olivine glomerocrysts (Figs. 9, 11). In contrast, oxide inclusions are exceedingly rare in *Type 1* olivines. Oxide minerals are not observed as phenocrysts in HMA but do occur in the groundmass as accessory chromian spinel. Based on detailed modal counts under reflected light, the stratigraphically lowest samples (MS-HMA2 and MS-HMA4) contain traces (50-100 grains/thin section) of very small (~10 μm) groundmass grains, whereas the stratigraphically highest samples (MS-HMA14 and MS-HMA15) contain slightly higher abundances (ca. 200-400 grains/thin section). Compared with crystallized

groundmass in typical basaltic to andesitic rocks (>1000 Fe-oxide grains/thin section) these are surprisingly low abundances.

Compositions of oxide inclusions vary with the specific enclosing mineral host. Within high-Mg pyroxene and olivine, oxide inclusions invariably are chromites or chromian spinels (Cr# = 80-45, Mg# = 75-45), whereas in Fe-rich pyroxene cores (Mg# < 75) ilmenite is the only oxide inclusion found (Supplemental Table A3). The highest-Mg# spinels occur in *Type 1* olivines whereas spinel inclusions in *Type 3* glomerocrystic olivines and within their opx dominated veinlets have intermediate Mg# (68-55) and Cr# (80-50). Spinel from a rare anhedral xenocrystic olivine-opx association (inset of Fig. 11a) has Mg# and Cr# at the low end of these ranges (55 and 50, respectively); these, and spinels from glomerocrystic *Type 3* olivine clusters, compositionally overlap with spinel from the nearby Trinity Ophiolite (Quick, 1981; Culeneer and Le Sueur, 2008). Finally, the lowest Mg# spinels (Mg# = 55-15, Cr# = 83-60) occur as inclusions in late-formed pyroxenes and olivines as well as in the groundmass (Fig. 11).

Plagioclase

Plagioclase occurs dominantly as groundmass crystals (or microphenocrysts). Only seldom does it occur as large phenocryst-sized crystals (≤ 1 crystal/thin section), except in the lowermost tephra deposits where both isolated grains and mono-mineralic glomerocrysts are slightly more common (a few crystals/thin section). Because all such grains are variably resorbed (i.e., mildly rounded to strongly sieve-textured) and somewhat variable in composition (An_{78-48}; Fig. 12), they are interpreted to be xenocrysts. Groundmass plagioclase is more uniform in composition (~An_{60}) and similar to rare inclusions in late-formed *Type 3* pyroxene (Fig. 12). Only a melt that has evolved during late stage crystallization can explain the groundmass plagioclase composition because the bulk composition of HMA has a Ca/Na ratio too high to crystallize An_{60} plagioclase. Groundmass composition (Table 2) would be in equilibrium with An_{68} plag (@ K_d=2; cf. Sisson and Grove, 1993); this suggests that groundmass plagioclase appeared even after some more cpx groundmass crystallization reduced the Ca/Na ratio sufficiently. Furthermore, only the highest observed An content of large crystals can be

401 potentially explained by equilibrium crystallization using a K_d value of 2. This is
402 consistent with textural observations indicating its xenocrystic nature.
403
404 **Proportion and distribution of pyroxene and olivine populations**
405 Volume proportions of essential minerals in the HMA magma, and distributions of all
406 distinctive phenocryst-sized pyroxene and olivine sub-types were determined by detailed
407 inventory for one representative thin section (sample MS-16-04). For simplicity, two
408 mineral populations were distinguished: grains [a] with maximum dimension greater than
409 200 μm, and [b] smaller than 200 μm (including some microphenocrysts). BSE images
410 and electron microprobe data were collected for all phenocryst-size pyroxenes except for
411 15 *Type 2* opx grains, for which identification was obvious from textural evidence. All
412 olivines were surveyed by textural criteria and compositional data were acquired on all
413 large olivines and a subset of smaller grains. On the other hand, only representative
414 pyroxene and olivine microphenocrysts were imaged by BSE and analyzed by electron
415 microprobe because they are so numerous. All surveyed pyroxene grains were classified
416 as discussed above and each type is distinguished in Figure 13. Results are also
417 presented in an interactive digital map that can be accessed at
418 (https://www.pdx.edu/geology/streck-Shasta-HMA) where BSE images along with
419 electron microprobe analyses are displayed. A high-resolution BSE image of the entire
420 thin section surveyed is found in Supplemental Figure A7.
421 Based on our detailed grain inventory, 'phenocryst-like' components in this sample
422 make up 18% by volume (after correction for 35% vesicularity); actually, these are nearly
423 all 'antecrystic' or 'xenocrystic'. *Type 1* and *2* pyroxenes dominate the population of
424 larger crystals. Estimated modal proportions (corrected for vesicularity) of phenocryst-
425 size minerals is: 20% Type 1 cpx and opx (Mg#75), 50% Type 2 opx (Mg#89), and 30%
426 Type 1 olivine (Fo_{93}). Among smaller crystals (< 200 μm), *Type 3* ('equilibrium') and
427 *Type 1* ('antecrystic') pyroxenes occur in subequal proportions, whereas *Type 2*
428 ('xenocrystic') crystals are less abundant. Notably, all pyroxene types appear to be
429 randomly distributed and well mixed at the thin section scale. Data on olivines indicate
430 that all distinctly large olivines are *Type 1* ('xenocrystic'), whereas the smaller grain

population is dominated by *Type 2* ('equilibrium') olivines. Implications of these findings are discussed below.

Trace element compositions of minerals and groundmass

Type 1 clinopyroxene crystals were analyzed for trace element content to further delineate the contrast between low Mg# core and high Mg# overgrowth and to estimate compositions of equilibrium melts that likely produced them. Representative analytical results are presented in Supplemental Table A5. Primary observations are that concentrations of incompatible trace elements are much higher in low Mg# cores than in high Mg# rims and overgrowths. Furthermore, REE patterns of low Mg# interiors indicate a pronounced negative Eu anomaly typically observed in evolved silicic igneous rocks (cf. Grove et al., 2005). And finally, melt compositions calculated with REE partition coefficients (Lee et al., 2007; Severs et al., 2009) yielded REE concentrations similar to or slightly higher than those of naturally occurring dacite lavas of Mount Shasta. Use of slightly higher partition coefficients calculated (cf. Brophy, 2008) for magmatic SiO_2 contents of Shasta dacites produces even closer agreement. Thus, the pyroxene cores are inferred to have crystallized from such magmas. We note that this is also the case for high-Mg basaltic andesite and andesite from the North Cascades (cf. Sas et al., 2017). In contrast, allowing for uncertainties in partition coefficients, estimated melts equilibrated with the pyroxene rims are similar in composition to HMA and consistent with in situ formation of these overgrowths.

Groundmass was analyzed at multiple areas of sample MS-16-04 and averaged results are listed in Table 2, where they can be compared to average analyses for melt inclusions from Ruscitto et al. (2011). Melt inclusions hosted by ~Fo_{87} olivines are similar (mostly within analytical uncertainty) to the average groundmass, and are herein designated as 'HMA-type'. In contrast, melt inclusions hosted in ~Fo_{93} olivines are of a distinctive 'primitive basaltic andesite' (or 'PBA') type (Ruscitto et al., 2011). The compositions of groundmass and HMA-type melt inclusions lie essentially on a hypothetical mixing line between Shasta basalts and dacites (cf. Fig. 1). Moreover, subtraction of phenocryst-size minerals in observed modal proportions (see above) from the bulk composition of sample

MS-16-04 indicates that this estimated 'liquid' is similar in composition to the analyzed groundmass and HMA-type melt inclusions.

The bulk composition of MS-16-04 (and all other HMA samples) differs from the groundmass composition with respect to elements that are concentrated in ferromagnesian minerals or diluted by their addition. That is, the groundmass composition is more silicic (61 wt.% SiO_2) and poorer in MgO, Sc, Cr and Ni. In detail, relatively incompatible elements (e.g., U, Th, Rb, Pb, Nb, Ta, Zr and LREE) are variably enriched by factors of 1.05 or greater, whereas less incompatible elements (including HREE and Y) are slightly depleted (cf. Table 2, where trace elements are listed in decreasing order of enrichment in the groundmass) relative to the HMA whole rock. These patterns are consistent with selective accumulation in the bulk magma of clinopyroxene, which has partition coefficients greater than unity for the latter elements.

Sr, Nd and Pb isotopic compositions

New Sr and Pb isotopic data for four samples are in close agreement with previously published data (cf. Table 1). Average isotopic values for HMA are as follows: $^{87}Sr/^{86}Sr$: 0.70301 ± 6; $^{206}Pb/^{204}Pb$: 18.873 ± 17; $^{207}Pb/^{204}Pb$: 15.588 ± 7; $^{208}Pb/^{204}Pb$: 38.463 ± 24. A single measurement of $^{143}Nd/^{144}Nd$ (0.51297) is available from Grove et al. (2002). These data lie within ranges for both basaltic and more evolved (andesite-dacite) lavas from Mt. Shasta ($^{87}Sr/^{86}Sr$: 0.7027-0.7038; $^{143}Nd/^{144}Nd$: 0.5127-0.5130; $^{206}Pb/^{204}Pb$: 18.75-19.18; $^{207}Pb/^{204}Pb$: 15.56-15.70; $^{208}Pb/^{204}Pb$: 38.32-39.05; cf. Supplemental Table A6 and Grove et al., 2002). Although these data may be considered representative of domains in the underlying mantle wedge, there is partial or near overlap with present day isotopic compositions of mafic and ultramafic rocks of the Trinity Ophiolite (cf. Supplement I; $^{87}Sr/^{86}Sr$: 0.7033-0.7160; $^{143}Nd/^{144}Nd$: 0.5123-0.5136; Gruau et al.1998; Jacobsen et al., 1984). Also, gabbro and ultramafic rocks from the nearby Castle Lake area (Schwindinger and Anderson, 1987) have $^{87}Sr/^{86}Sr$ (0.7044-0.7050) and Pb ($^{206}Pb/^{204}Pb$: 18.6-18.8; $^{207}Pb/^{204}Pb$: ~15.6; and $^{208}Pb/^{204}Pb$: 38.3-38.5) compositions close to those of Shasta area lavas (cf Supplemental Table A6). And, finally present-day Sr isotopic values for many Mesozoic age plutonic rocks of the nearby Klamath Mtns. are in the range 0.703-0.704 (Allen and Barnes, 2006). Detailed comparison of Sr-Nd-Pb

isotopic compositions of all these rocks is shown in Supplemental Figure A1. Thus, on the basis of these data, it is difficult to exclude involvement of such crustal rocks in Shasta area magmas, either via magma-wallrock interaction or by partial melting. In particular, magma interaction with ultramafic wallrocks would have small leverage on magmatic isotopic compositions considering the low concentrations of Sr, Nd, and Pb in such rocks.

DISCUSSION

The petrogenesis of the Mount Shasta HMA is at the forefront of the discussion of the origin and significance of HMA magmas in general (Kelemen et al., 2003; Grove et al., 2002; Streck et al., 2007a; Barr et al., 2007; Kelemen and Yogodzinski, 2007; Martin et al., 2011; Ruscitto et al., 2011, Mitchell and Grove, 2015; Walowski et al., 2016) and our data presented above bear strongly on this issue. We examine our data and those of other recent studies with the goal of evaluating scenarios to explain the observed chemical and mineralogical features of the Mount Shasta HMA. Specific petrogenetic scenarios that have been proposed include: [1] HMA represents a magma type that was derived more or less directly from the mantle with only minor modification by interaction with other magmas or with crustal rocks; [2] HMA is derived from a more mafic precursor magma via fractional crystallization ± open system processes like wallrock assimilation; [3] HMA is a product of magma mixing with some of the crystal cargo derived from the respective mafic and silicic mixing end members ± other contributions; and [4] HMA is a product of partial melting of crustal lithologies with the addition of some crystal cargo from other sources. The data presented here and in previous papers is used to assess the likelihood of these scenarios.

Origin of crystal and melt components in HMA

The diverse compositions and the complex textural relations of phenocryst-sized minerals in the Mt. Shasta HMA preclude the notion that the observed mineral assemblage formed by equilibrium crystallization of a single melt similar to HMA in bulk composition. Therefore, to understand the complex processes by which HMA was

assembled, we first need to consider the origins of the various mineral and lithic components and the processes that can be inferred from the petrographic and geochemical evidence. We begin with discussion of the latest stage of crystallization, immediately prior to eruption.

Late-stage crystallization – products from hybridized melt

Textural and compositional criteria clearly indicate that the latest-formed near-liquidus minerals in HMA are the *Type 3* pyroxene microphenocrysts and equivalent overgrowths (all with Mg# near 87 or slightly higher) on *Type 1 & 2* pyroxenes and the skeletal (or triangular inclusion-bearing) *Type 2* olivines and equivalent overgrowths (all near Fo_{87}) on *Type 1 & 3* olivines. These minerals clearly crystallized contemporaneously and shortly before eruption of the HMA magmas. This interpretation is supported by compositional overlap between rare spinel inclusions in these ferromagnesian minerals and in the groundmass (Fig. 11). Variation in Mg# and other elements (e.g. Cr) observed in *Type 3* pyroxene and in the zonation pattern of overgrowth of *Type 1* and *2* pyroxenes likely records melt evolution as olivine and pyroxene progressively crystallized during this late stage of crystallization. We infer that the ferromagnesian minerals crystallized from a common silicate melt having Mg# near 66 and evolving to a liquid near Mg# 60 (assuming bulk $K_d = 0.3$). Furthermore, this silicate liquid was saturated with regard to plagioclase only during the terminal crystallization period when groundmass crystals formed, and minimal oxide saturation is indicated by the sparse occurrence of Cr-rich spinels. The nature of this liquid is further constrained by compositions of melt inclusions in Fo_{87} olivines (Ruscitto et al., 2011), and by our analyses of interstitial groundmass (Table 2). Together, these constraints indicate that the late-stage melt component in the HMA magma is andesitic in composition, with specific characteristics as follows: ~62 wt.% SiO_2, ~5 wt.% FeO*, ~20 ppm Rb and ~60 ppm Cr, with Ba/Nb = ~70, La/Yb = ~11, and Sr/Y = ~76, (Table 2). We note that the groundmass composition would equilibrate with olivine of ~Fo_{87} assuming molar ferric iron fraction (X-fe3) = 0.22. Using the olivine-liquid thermometer of Lee et al. (2009), estimated magmatic temperature is ~1083°C on an anhydrous basis and close to 1000°C if magmatic water

553 content approached ~3 wt. percent (cf. Ruscitto et al., 2011). How this magma likely
554 formed is discussed below.

555 Textural and compositional observations support the notion that many disequilibrium
556 components observed in the HMA hybrid magma were assembled shortly prior to
557 generating the liquid for this *late-stage crystallization* and thus shortly prior to eruption.
558 For example, crystallization of late (micro)phenocrysts and formation of outermost
559 overgrowths is inferred to be rapid. The sharpness of interfaces separating core from
560 overgrowth in *Type 1 & 2* pyroxene and the similarities in compositional profiles for fast
561 (Fe, Mg) and slow (Cr) diffusing elements across this transition imply that the
562 overgrowths developed rapidly (Figs. 5, 6). Diffusional relaxation times were estimated
563 (cf. Costa at al., 2008) to simulate observed compositional profiles across the core-
564 overgrowth transition for selected pyroxenes depicted in Figure 6. For these calculations,
565 a temperature of 1100°C was assumed (based on our two-pyroxene geothermometry);
566 this is consistent with estimated entrapment temperatures for melt inclusions in Fo_{87}
567 olivine (Ruscitto et al., 2011). Calculations were made using the Costa spreadsheet
568 modified with diffusivities appropriate for clinopyroxene (Costa et al., 2008; Costa, pers.
569 comm.). Optimal fits were obtained for relaxation times on the order of a few months (~1
570 mo for pyroxene bP6, Fig. 6a; ~3 mo for pyroxene bP10, Fig. 6b). A short time scale for
571 magma interaction is also supported by [a] narrowness (~10 μm; cf. Fig. 5a) of euhedral
572 pyroxene and olivine selvages on earlier formed ferromagnesian minerals. These are
573 consistent with growth in ~100 days at realistic crystallization rates (ca. 10^{-10} cm/sec;
574 Cashman**,** 1993), and [b] development of hourglass zoning in pyroxene microphenocrysts
575 consistent with rapid crystallization of sub-alkaline magmas (cf., Brophy et al., 1999;
576 Skulski et al., 1994)

577 Restriction of plagioclase to the groundmass, and its absence as a phenocryst
578 indicates that the late liquid was undersaturated with respect to feldspar until groundmass
579 began to crystallize. This could be a consequence of elevated water content in the late-
580 stage magma, which is estimated to be about 3% (Ruscitto et al., 2011). Also, the
581 absence of oxide phenocrysts (and paucity of oxide minerals in the groundmass) suggests
582 that magmatic redox conditions were too reducing to stabilize these minerals earlier. This
583 observation is notable considering that redox conditions are near the fayalite-magnetite-

584 quartz buffer (i.e., already relatively reduced) for typical Cascades mafic lavas (Smith
585 and Leeman, 2005; Rowe et al., 2009).
586 In contrast, Ruscitto et al. (2011) estimate that selected melt inclusions record
587 relatively oxidizing redox conditions (oxygen fugacity near NNO+1.5 log units) based on
588 measurements of sulfur speciation. Under such conditions, we would expect HMA-like
589 liquids to be well saturated in oxide phases. This not evident from the observed mineral
590 assemblage and raises a question as to origin of the melt inclusions. We note that five of
591 six analyses of S speciation were made on melt inclusions from ca. Fo_{93} olivines, all of
592 which, according to our evaluation, are considered to be xenocrystic (cf. Ruscitto et al.
593 2011).
594
595 **Evidence for silicic (dacite) contributions - glimpses into the murky magmatic past**
596 Inference of precursor events and magmatic history must be gleaned from sparse
597 clues based on the population of 'non-equilibrium' crystals in HMA. *Type 1* pyroxenes
598 clearly represent a penultimate magmatic stage as, texturally, they post-date *Type 2*
599 pyroxenes. Fe-rich cores of *Type 1* pyroxenes provide direct evidence for involvement of
600 felsic melt components in HMA. However, variations in zoning patterns between
601 different subtypes indicate multiple contributions and a complex assembly history. *Type*
602 *1A* low-Mg# (59-75) pyroxene cores are consistent with their precipitation from melts
603 having Mg# between 30-47 (assuming bulk K_d near 0.3; Sisson & Grove, 1993). More
604 directly, compositions of rare melt inclusions in *Type 1A* pyroxene cores implicate a
605 parental liquid of roughly dacitic composition (Table 2). These melt inclusions provide
606 evidence that all low Mg# pyroxene (i.e., *Type 1A* cores) crystallized from silicic melts
607 with low FeO* and MgO contents (e.g. ~4 wt.% and ~1-2 wt.%, respectively), albeit our
608 estimated Mg#s are lower than those of typical Mt. Shasta dacites (cf. Grove et al., 2005).
609 Low Cr contents in *Type 1A* pyroxene cores (150-700 ppm in cpx and ~200 ppm in opx;
610 Supplemental Table A5) are also consistent with their formation from low-Cr liquids not
611 unlike Shasta dacites (that typically contain ca. 40-70 ppm Cr; Grove et al., 2005).
612 Furthermore, relatively low Al_2O_3 contents in these pyroxene cores imply that they
613 formed at low pressures (Fig. 16, see later discussion) and effectively preclude sub-
614 crustal storage and crystallization of the silicic host melt. Calculated REE patterns for

615 melts in equilibrium with low-Mg# cpx cores (Fig. 14) display large negative (ca. 0.8-
616 0.4) to negligible Eu anomalies. The negative Eu anomalies strongly implicate
617 involvement of feldspar in the generation of the melts from which *Type 1A* pyroxene
618 cores precipitated. Interestingly, such inferred silicic melts are more evolved (lower Mg#
619 and more fractionated REE) than observed for most Mt. Shasta dacites (Grove et al.,
620 2005). Nevertheless, some *Type 1A* cores as well as some *Type 1B & C* pyroxene cores
621 have compositions (e.g., Mg# ~75; REE systematics, Fig. 14) consistent with their
622 formation from melts similar to erupted Shasta dacites.
623 Another question concerns the progressive normal zonation observed in *Type 1B* & C
624 opx and cpx cores (Mg# varies between ~82-75 from interior to outermost part, except in
625 *Type 1B* that includes some portion with Mg# 75). This type of zonation is seemingly
626 consistent with progressive fractional crystallization of the host melt, but could also be
627 explained by mixing of the host melt with a more evolved (lower Mg#, essentially
628 dacitic) magma. The possibility that the Fe-rich cores were derived from disaggregated
629 cumulate or plutonic wall rocks rather than from a magma is considered unlikely based
630 on the presence of melt inclusions and the preservation of relict euhedral outlines in some
631 *Type 1* cores, both of which are consistent with their original formation as phenocrysts in
632 a silicic melt. These features, in combination with short time estimates for the
633 crystallization of high Mg# overgrowths, are consistent with crystal growth from dacitic
634 melt shortly before this magma mingled with other components to produce the final
635 HMA end product. We conclude that mixing to form the hybrid HMA involved two or
636 more distinctive and contemporaneous magmas in addition to entrainment of crystalline
637 wall rocks (cf. Ruscitto et al., 2011), to yield antecrysts of dacitic origin.
638 Finally, we note that similar petrographic and mineralogical features are not
639 uncommon, and have been interpreted in terms of injection of relatively hot mafic
640 magmas into crustal-level melt reservoirs or crystal mush zones beneath other arc
641 volcanoes (cf. Baggerman and DeBari, 2011; Price et al., 2012; Humphreys et al., 2013).
642 For example, iron-rich cores and complex reverse zoning in pyroxenes from Ruapehu are
643 consistent with mixing between mafic and more silicic magmas and/or reaction between
644 entrained 'dacitic' pyroxenes and invasive mafic magma (Nakagawa et al., 2002).
645

Evidence for incorporation of crustal-derived crystal cargo

As far as entrainment of crystalline wall rocks is concerned, we do recognize several distinct crystal populations that we consider unlikely to have been derived directly from magmatic sources. These are interpreted to be disaggregated xenocrystic debris of likely crustal derivation. In particular, it has been speculated that a possible source for such debris in Shasta lavas could be the Trinity Ophiolite that is inferred to underlie the Mt. Shasta area (cf. Baker et al., 1994).

Exotic pyroxenes.

Distinctive disequilibrium features (e.g., resorption channels and patchy zoning) in all *Type 2* opx crystals are taken as evidence for their derivation from coherent country rocks that were infiltrated by melt along cracks and grain boundaries. The pervasive presence of coarse spongy textures instead of a progressive increase in width and intensity of the resorption channels towards crystal rims are features consistent with melt infiltration. Compositions of the overgrowths and infillings (~En_{65}) implicate involvement of a significantly less magnesian melt than the late HMA host, but rather more like the inferred dacitic melt postulated to generate cpx with Eu anomalies. We suggest that features of *Type 2* pyroxene formed in a nearly solid (or crystal mush-like) environment prior to incorporation of *Type 2* pyroxenes into the same magma where *Type 1* pyroxenes resided. Subsequent crystallization of high Mg# overgrowth on both *Type 1* and *2* pyroxenes ties these crystal populations together and suggests that the enveloping melt was initially slightly more magnesian than melt inclusions within Fo_{87} olivines (Ruscitto et al., 2011) or the HMA groundmass in order to explain beginning rim overgrowth with Mg# >87 (Table 2; Figs. 5, 6). We note that REE element patterns and incompatible element concentrations of HMA and those of Mt. Shasta dacites (Fig 14; Tables 1, 2) are nearly indistinguishable and overlap with those inferred from *Type 1* pyroxenes. These observations allow the interpretation that the bulk magma was essentially dacitic prior to the final hybridization/mixing assembly that produced the HMA (i.e., increased MgO, Cr, and Ni and subtly decreased Si, and other incompatible elements).

Exotic olivines.

A country rock origin is also inferred for *Type 3* olivine clusters. Irregular crystal interfaces and diverse optical orientations of the aggregate grains suggests that these inclusions are micro-xenoliths akin to those observed macroscopically in hand sample. Disaggregation of the xenoliths accounts for isolated grains having similar composition and morphology. The abundance and distinctive (for most) compositions of spinel grains in cross-cutting opx-rich intergranular seams (Figs. 9, 11b) is notable considering the paucity of spinels in HMA, and these features support an exotic origin for the micro-xenoliths (Fig. 10). Compositions of *Type 3* olivines are intermediate between *Types 2 and 1* olivines, but similar to those of many primitive Cascades basalt phenocrysts (Conrey et al., 1997; Smith and Leeman, 2005; Rowe et al., 2009). Thus, they could be derived from olivine-rich cumulate sequences beneath the Cascades arc – either in the underlying crust or upper mantle – or from underlying accreted mafic-ultramafic bodies such as the Trinity Ophiolite (e.g. Quick, 1981). Considering that the modern Cascade volcanic belt rests on a stack of accreted convergent margin terranes of Paleozoic to Mesozoic age, there could be many sources for the lithic debris found in HMA and other Mt. Shasta lavas (cf. Grove et al., 2005; Snoke and Barnes, 2006).

Type 1 olivines are also considered to be exotic based on their conspicuously large size, their anhedral to subhedral (and sometimes fragmental) morphology prior to development of late euhedral overgrowths of Fo_{87} olivine, and their highly refractory composition (~Fo_{93}). Such Fo_{93} olivines largely plot outside the Sobovev et al. (2005) field for olivines in mantle-derived rocks (cf. Fig. 10). These features distinguish them from all other olivines in HMA (and in all other Shasta lavas as far as we are aware), and rule out an equilibrium relationship to the late hybrid melt. Recent discovery of rare melt inclusions with compositions distinct from the late-stage host melt (Ruscitto et al., 2011) and lower $\delta^{18}O$ values compared to other minerals in HMA (Martin et al., 2011) led these authors to support our xenocrystic interpretation (cf., Streck et al., 2007a). However, the origin of these olivines (and their melt inclusions) remains enigmatic.

We doubt that these olivines are true phenocrysts precipitated from any known mafic magma in the Shasta area. If magmatic, their forsteritic composition would imply formation from a liquid with very high Mg# (near 84, assuming K_d = 0.3 and normal redox conditions), and such melts could only be derived from a highly refractory source

not commonly recorded in mantle-derived xenoliths. Highly forsteritic olivines have been found elsewhere, and attributed to formation from highly oxidized magmas wherein much of the iron occurs as Fe^{3+} (e.g., Cortes et al., 2006; Blondes et al., 2012). However, highly oxidizing magmatic conditions would favor precipitation of magnetite-rich spinels and, as noted earlier, spinel inclusions are rare in *Type* 1 olivines and would not be consistent with the precipitation of the observed sulfides (Stone et al., 1989). Alternatively, highly forsteritic olivines (up to ~Fo_{96}) can form by prograde heating of serpentinite (e.g., Vance and Dungan, 1977; Evans, 2008) in which much of the protolith iron is oxidized and sequestered in secondary magnetite segregations. So, another possible source is from entrainment of (or melt reaction with) serpentinite bodies in the underlying crust. This scenario is supported by the redox state of melt inclusions in *Type 1* olivines (as discussed above).

Relict plagioclase – further evidence for evolved components.

The sparse occurrence of strongly resorbed grains and aggregates of phenocryst-sized plagioclase within tephras of the Whaleback Quarry further implicates involvement of evolved magmas and/or plutonic contaminants in HMA magma. We note that observed plagioclase compositions overlap those in Shasta dacites, whereas they are generally too An-poor to have recrystallized from a melt with Ca/Na similar to that in HMA (Fig. 12).

Comparison of observational and experimental petrology of HMA

Despite overwhelming evidence in support of a hybrid or mixing origin for HMA as presented here and proposed in earlier studies (Anderson, 1974; Streck et al., 2007a, b, c), it is instructive to review and contrast the observed mineral assemblage with phases produced experimentally from HMA melt composition (Müntener et al., 2001, Grove et al., 2003, 2005). Experiments have been conducted over a range of conditions spanning uppermost mantle (i.e., 1.5 and 1.2 GPa; Müntener et al., 2001; Grove et al., 2003) to crustal conditions (800-0.1 MPa; Grove et al., 2003). The starting material used in most experiments is sample 85-41c, which is nearly identical in composition to our sample MS-HMA11 (Fig. 3c, Table 1). However, experiments at 1.5 GPa used a modified HMA composition to which an excess of 2.5% FeO was added (Grove et al., 2003).

739 If a natural partial melt of HMA composition crystallized during ascent to the surface,
740 it is reasonable to expect that observed phenocrystic mineral phases and compositions
741 should correspond with those produced at appropriate experimental conditions. Figure 15
742 (also see Fig. 1) illustrates the experimental liquid line of descent with which we compare
743 our mineral database.

744 As a general rule, near-liquidus mineral assemblages for all high-pressure (1.2, 1.5
745 GPa) experiments comprise only pyroxenes (opx ± cpx) whereas low-pressure
746 experiments produced mostly olivine, opx or cpx, plus spinel or plagioclase or no Al-rich
747 phase. Both opx and cpx (with Mg# ≤ 86) crystallized in low pressure experiments along
748 with plagioclase after residual liquid SiO_2 content exceeded ~59 wt.%. In most cases the
749 experimental mineral assemblage does not correspond with the natural assemblage (e.g.,
750 olivine or a pyroxene is missing, or plagioclase is present). Only one 200 MPa run, with
751 75% liquid remaining, closely replicated the observed liquidus assemblage olivine + opx
752 + cpx + spinel (Fig. 15a). However, in this example, Mg#s (82-84) for the experimental
753 pyroxenes and olivine are lower than observed in the natural minerals (Fig. **15b**). No
754 experimental olivine comes close to the Fo_{93} composition of *Type 1* olivines. Natural
755 pyroxenes also have significantly higher maximum Cr_2O_3 contents than any experimental
756 ones (Fig. 16). Al_2O_3 contents for high-Mg# (>82) pyroxenes are comparable except for
757 those in the 1.5 GPa experiment. We note that only low-pressure experiments reproduced
758 naturally observed Al contents for low-Mg# pyroxene cores (Fig. **16**). Although we
759 argue here that the cores cannot have crystallized from HMA magma, this observation is
760 consistent with low-pressure conditions for their formation.

761 It is particularly noteworthy that oxide inclusions in *Type 1* pyroxene cores are
762 ilmenites whereas oxide phases that crystallized in HMA experimental liquids (e.g., 61.7
763 wt.% SiO_2 melt of HMA #85-41c; Grove et al., 2003) are chromian spinels; such spinels
764 also occur in the actual HMA groundmass (Fig. 11). This evidence indicates that *Type 1*
765 pyroxene cores are not genetically linked to a HMA parent or its derivative liquids. They
766 are most plausibly derived from dacitic liquids of unrelated origin. Spinels appear to be
767 generally sparse in the experiments, as is also the case for the natural samples we have
768 examined. Spinels in one 200 MPa experiment are compositionally similar to spinel
769 inclusions that occur in late crystallizing (i.e., phenocrystic, Mg# ca. 87) olivine and

pyroxene as well as groundmass spinel. On the other hand, no experimental spinels are similar to those included in Fo_{93} olivines (Fig. 11). Finally, plagioclase is only common in relatively evolved experimental melts or at low (near-surface) pressure. This jives with the observation that 'equilibrium' plagioclase in natural HMA is restricted to groundmass crystals.

Overall, most of the experiments fail to replicate first order mineral compositional or assemblage features documented in the natural samples. Specifically, they do not support the premise that the observed mineral assemblage could be in equilibrium with a melt of HMA composition. This is not surprising considering the documented presence of clearly xenocrystic minerals in HMA.

Evidence from melt inclusions

Two recent studies investigated melt inclusions in olivines from the HMA (Ruscitto et al., 2011), and from high-alumina olivine tholeiites (HAOT), calcalkalic basalts, and basaltic andesites (BA) from the Mt. Shasta area (Le Voyer et al., 2010). Ruscitto et al. (2011) discerned two melt components in HMA minerals. A low-Ca (or HMA-like) component is trapped in *Type 2* (~Fo_{87}) olivines and thus is considered representative of the melt from which all late-stage phenocrystic or overgrowth minerals crystallized. The average composition of such melt inclusions is slightly more magnesian than HMA groundmass, but has incompatible trace element abundances similar to those in our HMA groundmass average (Table 2). After correction for post-entrapment crystallization (PEC) to the host olivine composition (ca. Fo_{87}), olivine equilibration (trapping) Ts are calculated to be near 1150°C for these inclusions (cf. Supplement B, Fig. B3). A second high-CaO melt component (primitive basaltic andesite, or PBA) is restricted to inclusions in *Type 1* olivines (ca. Fo93), and differs from all other bulk lava or melt inclusion compositions so far recognized at Mt. Shasta (Figs. 1, A6). After PEC-correction to the host olivine composition, compositions of these inclusions correspond to higher trapping Ts (~1190-1260°C, assuming X-fe3 = 0.15; cf. Supplement II). This PBA melt component is also distinguished by relatively high concentrations of H_2O (maximum ca. 3.5 wt.%), Cl (>0.2 wt.%) and Sr (most >1000 ppm), but low contents of Ba (most <100 ppm), K (ca. 0.3 wt.%), and other incompatible elements (Supplemental Fig. A6); Cl/K

ratios (ca. 0.9) are distinctly higher than observed in melt inclusions from Shasta basalts (<0.2; Le Voyer et al., 2010). We also note that PBA melt inclusions are heterogeneous in composition, with large variations in major elements (SiO_2, MgO, CaO, Al_2O_3, etc.), Cr (ca. 200-4000 ppm), Sr (860-1200 ppm), and B (2-40 ppm) (cf. Supplemental Figs. A3, A6). Considering the elements K, Ti, and P (all of which are incompatible in olivine), we note that the PBA inclusions have distinctly higher P_2O_5/TiO_2 (ca. 0.5) and lower K_2O/TiO_2 (ca. 0.6) ratios than observed in either the HMA-type inclusions or HMA bulk lavas or groundmass (ca. 0.2 and 1.2-1.5, respectively, Supplemental Fig. A5). Because these ratios should not be affected by corrections for post-entrapment crystallization, they provide robust evidence for the exotic nature of the PBA component. The average PBA major element composition is considered similar to experimental hydrous melts in equilibrium with harzburgite (Ruscitto et al. 2011). Also, given their compositional distinctiveness, the source(s) of PBA-like melts must differ from sources for other known mafic magmas in the vicinity of Mt. Shasta (e.g., basaltic andesite [BA] and high alumina olivine tholeiite [HAOT] melt inclusions of Le Voyer et al., 2010).

According to the latter authors, the nearly anhydrous (<0.1% H_2O) HAOT inclusions are interpreted to represent melts of a relatively dry lherzolite mantle source. In contrast, the relatively hydrous (ca. ≥1.5% H_2O) BA inclusions are attributed to melting of a more depleted mantle source that previously had been metasomatized by subduction fluids and melts (thus stabilizing amphibole). Trapping Ts for HAOT- and BA-type inclusions are estimated to be near 1330°C and 1250°C, respectively. Leeman et al. (2005) deduce similar segregation Ts for Shasta basaltic lavas at uppermost mantle depths, and infer that HAOT source domains reside deeper in a compositionally stratified mantle. Ruscitto et al. (2011) estimate that PBA melts were trapped at Ts between 1200-1280°C – consistent with our calculations as noted above. Thus, if BA- and HAOT-type magmas result from shallow melting of the mantle it is unclear where the alleged PBA source fits in spatially and compositionally.

We recognize that mantle heterogeneities may exist at relatively small scales allowing proximal magmas to acquire a spectrum of distinctive mantle signals (cf. Conrey et al., 1997, Borg et al., 2002; Leeman et al., 2005). But if source differences are attributed to variable enrichments by subduction-related fluids, a more important issue concerns why

the PBA melt source is selectively enriched in some (e.g. Sr, Cl) but not all (e.g. Ba, K, Rb) fluid-mobile elements (cf. Supplemental Fig. A6). A possible explanation is that the melt inclusions reflect inherent heterogeneities associated with accretion of arc terranes in this region, which formed intermittently since the early Paleozoic, such that specific melt compositions likely depend in detail on protolith composition. In this case, the PBA protolith appears to have affinities with some serpentinites and/or seawater-altered oceanic crustal rocks. Furthermore, we can envision that potential melt sources (mantle or crust) may evolve over time due to successive melt extraction (i.e., depletion) vs. metasomatic (i.e., selective enrichment) 'events'.

As an alternative origin for the PBA inclusions that is consistent with their unusual composition, we suggest that they could be products of melt interaction with accreted and hydrated ultramafic basement terranes comprising water- and Mg-rich phases like serpentine, tremolite, and magnesite. Melting of these materials at some scale could be triggered by intrusion of hot mafic magmas at appropriate crustal depths as documented in the roots of exposed volcanic arc/subduction complexes (e.g., DeBari et al., 1999; Greene et al., 2006; Horodyskyj et al., 2009). We predict that such melts could be moderately water-rich (if formed at sufficiently high pressure, say in the deep crust), highly magnesian, and could mix with the intrusive magma to produce PBA-like liquids that, in turn, could be trapped in highly forsteritic olivine formed under relatively oxidizing, prograde metamorphic conditions (cf. Vance and Dungan, 1977) within a wall-rock aureole. Furthermore, such melts need not be volumetrically significant. Thus, we postulate that *Type 1* forsteritic olivines with their unique PBA-type melt inclusions could be derived from disaggregated wall-rocks and entrained in the compositionally distinct HMA magma – perhaps shortly before its eruption (so as to allow growth of the thin reaction rims of Fo_{87} olivine).

This scenario is consistent with several observed features. For example, if serpentinized ultramafic massifs undergo prograde metamorphism, it has been shown in numerous cases that the resulting olivine can be extremely forsteritic (e.g. Evans, 1977, 2008; Padrón et al., 2010); this could explain the unusually high Fo content and mostly anhedral habit of the olivine mineral hosts of the PBA inclusions. In this regard, and considering their heterogeneous nature, the melts may have never been in equilibrium

with Fo_{93-94} olivines; if so, correcting original PBA inclusions by adding on average 20% olivine back to reach equilibrium with the host olivine (cf. Ruscitto et al., 2011) could be excessive. Furthermore, fluids derived from such massifs can be chlorine-rich if they originally were derived from seawater-altered rocks (e.g. Scambelluri et al., 2001; Garrido et al., 2005; Kodolányi and Pettke, 2011), and this could explain the high Cl (and Sr) content of the high-Ca (PBA) inclusions found in *Type 1* olivines (Supplemental Fig. A6). It is noteworthy that there are no known occurrences of erupted PBA-like lava, whereas BA and HAOT lavas are relatively common near Shasta and elsewhere in the modern Cascades; thus, there is no compelling reason to believe that magmas with PBA-like compositions are volumetrically significant.

Generation of the silicic end member (and other Shasta dacites)

Compositions of Fe-rich pyroxene cores and the melt and mineral inclusions they host (Anderson, 1974; Stone et al., 1989; Streck et al., 2007a; Ruscitto et al., 2011; this study) implicate involvement of silicic (dacitic) magma as an essential component in forming HMA. Thus, the manner by which the dacites formed is relevant to discussion of the HMA. Specifically, what is the nature of the evolved melt component in HMA, and what is its relationship to other evolved magmas in the vicinity of Mt. Shasta? Although they clearly recognized that most Shasta dacites and andesites are to some degree mixed magmas, Grove et al. (2005) proposed that they are products of moderate pressure (near water-saturated) fractional crystallization predominantly derived from high magnesian andesite and, to lesser extent, more mafic mantle inputs. This interpretation is stressed in subsequent papers (e.g., Magna et al., 2006; Martin et al., 2011). As previously discussed (also see Fig. 1), the experimentally determined liquid lines of descent or phase assemblages do not provide conclusive support for this view, and several other processes are also inferred to be important – most notably, magma mixing as evidenced by heterogeneous mineral populations and textural relations in most samples.

The latter view is consistent with independent geochemical evidence. For example, U-series and trace element analyses of Shasta lavas (Newman et al., 1986; Volpe, 1992) strongly implicate magma mixing processes in their formation, and define distinct mixing relations associated with each growth stage of the volcanic complex. The U-series data

are notable in that they show relative enrichments of [^{230}Th/^{232}Th] with respect to [^{238}U/^{232}Th] (here, square brackets indicate activity ratios). This is significant because (1) the isotopic disequilibria imply recent disturbances in the U-series systematics of the magma sources, (2) the lack of significant ^{238}U-enrichment in Shasta (and other Cascades) lavas seemingly precludes involvement of recently extracted subduction zone fluids (whereas many young lavas from other volcanic arcs do show significant ^{238}U-enrichment; cf. Turner et al., 1997; George et al., 2004; Zellmer et al., 2005), and (3) varied ^{230}Th-enrichment in the respective mixing end members may be related to dynamic melting processes unrelated to subduction per se. In particular, the second point implies that input of subduction zone fluid is relatively low for the Cascades in general, and this can be attributed to the unusually warm thermal structure of this arc (cf. Harry and Green, 1999; Green and Sinha, 2005; Leeman et al., 2005; Walowski et al., 2015).

As seen in our Figure 1, the Shasta lavas define relatively strong near-linear arrays in plots of major element oxides vs. SiO_2, albeit there is notable diversity among the mafic lavas – as observed at most Cascades volcanoes (cf. Leeman et al., 1990, 2005; Bacon et al., 1997; Borg et al., 1997). Nevertheless, these arrays form 'chords' connecting mafic (basaltic) and silicic (dacitic) end member compositions on otherwise curvilinear trajectories defined by loci of relevant experimentally produced fractionation/melting liquids. These chords approximate linear mixing arrays analogous to those observed for the 1915 Lassen eruption, that are attributed to mixing of basaltic and dacitic magma end members (Clynne, 1999). These relations imply the coeval existence of distinct reservoirs of mafic and evolved magma that can comingle and mix in a fairly reproducible manner. Some scatter is to be expected in plots that represent multiple eruptive stages over extended duration (ca. 250 ka for Shasta; Christiansen et al., 1977), because the nature of the mixing end members may vary to some degree over time. Importantly, the HMA groundmass (or near-equivalent melt inclusions) lies close to the main Shasta arrays as defined by basalts, andesites, and dacites, whereas the bulk HMA lava compositions diverge from the Shasta arrays in a manner consistent with entrainment of xenocrystic materials (largely olivines and pyroxenes) of ultramafic provenance as noted earlier (cf. Streck et al., 2007a). In our view, the relict vestiges of dacite affinity

(e.g., the Fe-rich pyroxene cores) are inherited from dacitic magma(s), the bulk of which were otherwise assimilated by hot mafic liquids to produce the HMA magma.

However, the compositional spectrum of Shasta dacitic lavas is characterized by a wide range in trace element concentrations that precludes a simple petrogenesis for such magmas. For example, over a narrow range of SiO_2 (62-64 wt.%) Sr and Ba concentrations in Shasta dacites range more than twofold, and are negatively correlated (Fig. 17a); andesitic compositions overlap but are more scattered. To model the dacite array by fractional crystallization (FC), a high degree of fractionation (>50%) is required and plagioclase must contribute throughout to maintain a sufficiently high Sr bulk partition coefficient (>1) to account for decreasing content of this element. This process could also lower Sr/Y progressively (Fig. 17b) because Sr content decreases while Y content remains near constant or increases slightly. Thus, if the dacites evolved in this manner, it is implicit that parental dacitic magmas must initially be characterized by elevated Sr and Sr/Y ratios. However, there would also be a significant concomitant increase in SiO_2, which is inconsistent with the narrow SiO_2 range for the dacite array. There is no quartz, alkali feldspar, or low An plagioclase (< An_{20}) in any of the Shasta dacites (cf. Grove et al., 2005) that could contribute to buffering the SiO_2 of bulk rock within the 62-64% silica window during the required high degrees of fractionation to explain the dacite array. It has been proposed that such magmas could form either by partial melting of subducted oceanic crust (Kay, 1978; Drummond and Defant, 1990), or by melting mafic amphibolite protoliths in the deep crust (e.g., Smith and Leeman, 1987; Baggerman and DeBari, 2011; Qian and Hermann, 2013).

Alternatively, the nearly fourfold range in dacite (or andesite) Sr/Y values could partly reflect source heterogeneities (i.e., different protoliths or different depths of melting; cf. Gao et al., 2016 for review), resulting in high- and low-Sr variants (also seen at Crater Lake; Bacon and Druitt, 1988). In this case, the near-linear trends in Figure 17 could reflect mixing of diverse dacitic magmas within a complex storage/feeder system at depth.

Other evidence against a sole fractionation control on compositional variations of Shasta dacites is the sub-vertical trend in a Sr vs. Al_2O_3 diagram defined by dacites and all basaltic Shasta magmas that could potentially serve as fractionating parental magmas

(Supplemental Fig. A6). Plagioclase-free fractionation at greater crustal depth could enhance Sr but, in this case, derivative compositions would not trend vertically but rather towards increased Al_2O_3 content. Secondly, if plagioclase is removed at shallower depth, vertically decreasing Sr trends would be unlikely as well (cf. Grove et al., 2005). Considering these difficulties in explaining the dacite arrays solely in terms of magma fractionation, it seems that partial melting processes are implicated in generating Mt. Shasta dacitic magmas.

Dacitic magmas at other Cascades volcanoes (and many other places) commonly are interpreted to be partial melts of crustal lithologies such as amphibolites (e.g., Smith and Leeman, 1987; Borg and Clynne, 1998; Baggerman and DeBari, 2011). Hence, partial melting scenarios to produce dacite magmas at Shasta are a viable alternative (or at least complementary) to fractional crystallization (cf. Lopéz et al., 2005; Qian and Hermann, 2013), particularly if large volumes of mafic magma stagnate in the lower crust (cf. Tiepolo et al., 2011, 2012; Yu and Lee, 2016). A notable feature of Mt. Shasta dacites is that they mostly have high Mg# (ca. 54-64, except a few at Mg# ~25; Grove et al., 2002, 2005). It could well be that high Mg# is a reflection of the source protolith, possibly enhanced by higher oxygen fugacity (cf., Sisson et al., 2005; Gao et al., 2016). Protolith and partial melting conditions may vary so as to produce relatively silicic melts with varied trace element contents. For example, slight positive correlation between Mg# and Sr, and a negative correlation with Ba in Shasta dacites might suggest that high Sr, low Ba dacites are derived from higher Mg# protoliths and vice versa.

Oxygen isotope constraints on formation of HMA

Controversy over the significance of Shasta HMA has encouraged alternative approaches to understand the origin of this (and similar) magma. For example, Martin et al. (2011) measured oxygen isotopic composition of olivines and pyroxenes from several HMA samples as well as other Shasta basaltic and dacitic lavas. Unfortunately, mineral bulk composition (i.e., Mg#) is not available for the specific samples (usually aggregates of several grains) analyzed for $\delta^{18}O$. Melt-equivalent $\delta^{18}O$ values calculated from the mineral analyses for HMA (6.6-6.9‰) partly overlap with those for HAOTs (6.7-6.9‰) and BAs (6.3-6.7‰), and are lower than values for dacites (7.2-7.4‰). All of these

values are considered higher than expected (ca. 5.5-6‰) for 'normal' mantle-derived magmas, and this is taken to reflect input of ^{18}O-enriched components from the subducting slab in this region (Martin et al., 2011). In contrast, a more detailed investigation of the nearby Mt. Lassen volcanic field concluded that elevated δ^{18}O values there (~5.8-6.6‰ for basaltic lavas and ~6.0-8.3‰ for more evolved lavas) primarily reflect assimilation or melting of preexisting crustal rocks, and that intrusion of mafic magmas resulted in hybridization of the preexisting crust (Feeley et al., 2008). Of particular relevance to our study, the overlap of estimated compositions for mafic melts seems permissive of some mixing between basaltic and dacitic magmas, particularly if the precursors to the basaltic lavas had normal mantle δ^{18}O values (ca. 5.5 to 6‰). Data reported for only two 'xenocrystic' HMA olivines (4.8-5.0‰) are lower than for olivines from other Shasta mafic lavas (5.3-5.8‰ for BAs, and 5.9-6.1‰ for HAOTs). Because compositions of rocks and minerals from the Trinity Ophiolite range widely (4 to 10‰; Lecuyer and Fourcade, 1991; Martin et al., 2011, and references therein), the xenolithic olivines could be derived from such sources. However, given the latitude in end member compositions, we conclude that the oxygen data cannot adequately resolve mixing relations in the Shasta HMA. Furthermore, considering the work of Feeley et al. (2008), the role of crustal contributions at Shasta may be underestimated.

Possible mixing scenarios to yield Mt. Shasta HMA

In an attempt to quantify the mixing relations that produced HMA magma, several scenarios were evaluated using major element compositions of hypothetical mixing components. In reality, the number of components that have been discerned as well as variability (and in some cases, uncertainty) in their compositions makes it difficult to precisely accomplish this goal. The basic model to be tested concerns the proposition that HMA liquid is a mixture of some basaltic magma with a dacitic magmatic component. The latter appears to be the source of very high Sr in HMA. Also, the bulk HMA magma appears to have contributions of an ultramafic nature to account for observed xenocrystic crystals and also high contents of transition metals. In practice, for this component we used a composite ultramafic component comprising the average of Trinity Ophiolite samples with more than 37% MgO using data from the literature

(Jacobsen etal., 1984; LaPierre et al., 1987; Gruau et al., 1998) combined with three samples from Castle Lake area (cf. Supplemental Table A6). Initial models were tested by systematically involving all variants of basaltic lavas from the Shasta region, coupled with average dacite, and then the dacite components were broken down into averages for each of the four eruptive phases of Mt. Shasta (cf. Grove et al., 2002, 2005).

Conceptually, we envisioned that injection of a specific type of basalt into a reservoir of dacitic magma could trigger a mixing process and perhaps related eruption event as proposed for many other volcanoes. Also included in the models were dominant crystal types observed in HMA samples, either as phenocrysts or xenocrysts. Combinations of these components were incorporated into a linear mixing algorithm and mixing proportions determined that provided optimal fits to the target composition of HMA, its groundmass, and the HMA-type melt inclusions. Optimization was achieved by minimizing the sum of the squared residuals using the SOLVER tool in Excel (cf. Herrmann and Berry, 2002). A drawback to this approach is that the matrix solutions can be rapidly overdetermined if the number of components exceed ~50% of the number of elements used in the models, in which case solutions are not reliable. So, after initial screening of potential mixing components, the number used in any given model was restricted to five or less. In practice, this was accomplished by omitting minor mineral phases that contributed little to the target composition, or that effectively mimicked contributions of similar components (e.g., olivine or pyroxene variants).

Initial results indicate that optimal fits could be obtained using a calcalkalic basalt variant (represented by sample 85-44; cf. Grove et al., 2002); the HAOT variants produced inferior fits. For the dacite end member, all of the aforementioned averages were tested, as they varied in subtle ways and it is clear from the similarity in REE (and other incompatible element) contents of HMA and the dacites, that they likely were a dominant ingredient in HMA. The most successful models are summarized in Table 3. All have low values for $\sum R^2$ (most < 0.5), and thus closely reproduce the target compositions. However, nature is vastly more complex that our simple models. Thus, we stress that these solutions are sensitive to the specific choice of mixing end members and to the hypothetical scenarios being tested. Principal observations are that the HMA groundmass (i.e. devoid of phenocrysts or xenocrysts) can be modeled essentially by

mixing basaltic (CAB) and dacitic magmas, with roughly 80-84% dacite depending on the average composition used. Here and with other scenarios, use of the average dacites of Sargents Ridge age produces distinctive results with greater proportion of dacite, but also poorer least-squares fits; for this reason they are considered least likely (also note that they have distinctively higher $^{87}Sr/^{86}Sr$ than than HMA; cf. Supplemental Fig. A1). Basalt proportions range from about 13-20%, and the most successful models include addition of Type 2 cpx (~8%) and removal of xenocrystic Type 1 olivine (~5%). Models for the HMA-type melt inclusions indicate that they can be reproduced by mixing of basalt and dacite in subequal proportions with small additions of cpx and loss of olivine. However, these models have consistently poorer fits, and this could reflect systematic differences in the compositional data (obtained by different methods) as well as the heterogeneity of the melt inclusions. Finally, HMA whole rock compositions are best modeled by combination of dacite (~56%) and basaltic (~30%) magmas plus ultramafic material (~5%) and Type 2 pyroxene (~8%); $\sum R^2$ values for these models are among the best obtained. In summary, the proposed mixing scenarios can reasonably account for bulk compositions of HMA products, and confirm a dominant contribution of dacitic material to the mixtures.

As an independent test of these results, we used the predicted mixing proportions and concentrations of nominally incompatible elements in the mixing components to simulate the trace element compositions of HMA products. We avoided use of transition metals in this exercise because their concentrations are highly variable and difficult to constrain for many of the model end members. Comparisons between calculated and observed compositions are shown for all models (excluding those with Sargents Ridge dacite) in Figure 18. Overall, average misfits are about 15% for the HMA WR and groundmass models, and 22% for the melt inclusion model. Because uncertainties on the target compositions are almost as large, these are considered to be successful fits. The largest misfits are for Rb, Sr, Th and U, and they could be rectified in large part by using a handpicked dacite composition in the models. In conclusion, compositions of the HMA variants are readily reproduced by plausible mixing scenarios.

Summary interpretation of HMA origin

The high-magnesian andesite from the Mt. Shasta area contains a complex array of equilibrium and disequilibrium mineral components. Based on the aggregate information now available, the HMA clearly represents a hybrid mixed magma as proposed by Streck et al. (2007a). It cannot be considered as a primitive direct melt from the mantle, but how far removed it is remains an important point of contention. Nor does the petrologic or experimental evidence support the formation of HMA simply by differentiation of mafic parental magmas. Its origin is most plausibly the result of mixing between mafic and silicic magmatic components coupled with contamination of crustal wallrocks. The felsic magmatic components could in part be products of melting of previously emplaced or underplated mafic magmas in the lower crust or uppermost mantle.

The earliest discernable components are attributed to formation and crystallization of silicic (dacitic?) magma as recorded by pyroxene crystals with low Mg# cores and by rare melt inclusions in these cores. Normally-zoned cores of *Type 1* pyroxenes could signify that the host magma evolved from a more mafic liquid and/or interacted or mixed with more evolved magmas. Considering the low-Al contents of the pyroxenes and evidence for entrainment of disaggregated melt-infiltrated country rocks, we infer that these magmas resided in a crustal reservoir and that the country rock comprised abundant opx and olivine (i.e., harzburgite to dunite protoliths). Some of the dacitic melt (or precursors thereof) infiltrated ultramafic(?) country rock leading to pervasive resorption, patchy zoning, and occasionally low-Mg# overgrowths on orthopyroxene. Mobilization of selvages of altered and resorbed country rock dispersed abundant xenocrysts (estimated as 1/3 of all single crystals in HMA), micro-xenoliths and any partial melt that resulted from mineral breakdown reactions. Many of the entrained crystals have been disaggregated and comminuted during transport. This mobilization was possibly facilitated by recharge of new mafic magma. Subsequent mixing between resident evolved magmas, country rock-derived crystal debris, and possibly newly emplaced mafic magma can account for the final bulk composition and petrologic character of the erupted HMA magma. Late-stage cooling of interstitial liquid in this magma can explain the presence of skeletal to more euhedral *Type 2* olivines, nearly unzoned *Type 3* pyroxene phenocrysts, and high-Mg# overgrowths on previously entrained 'dacite-derived' and 'country-rock-derived' pyroxenes and olivines. This final crystallization

interval must have occurred shortly prior to (and perhaps contemporaneous with) final magma ascent, and preceded eruption by months at most.

IMPLICATIONS

Basaltic magmatism in volcanic arcs is widely attributed to melting of mantle domains variably modified by inputs of fluids or melts derived from subducting oceanic crust and/or sediments. Globally, there is considerable diversity among such magmas – ranging from almost MORB-like low-K tholeiitic compositions to a spectrum of more potassic calcalkalic and even alkalic compositions (cf. Gill, 1981). In the Cascades and several other arcs, basalts of OIB affinity are common (Leeman et al., 1990, 2005; Bacon et al., 1997; Conrey et al., 1997; Righter, 2000; Green, 2006; Rowe et al., 2009). Such diversity may stem from many factors, but for the Cascades two distinct generic interpretations have been favored. One camp sees the compositional spectrum as essentially the product of flux-melting with the strength of calcalkalic signatures increasing with magnitude of aqueous flux addition to the source (cf. Borg et al., 1997; Reiners et al., 2000; Rowe et al., 2009). Alternatively, Leeman et al. (2005) suggested that the mantle wedge may be compositionally stratified, with low-K tholeiites and OIB-like basalts derived from little-fluxed domains in the deeper convecting asthenospheric part of the mantle, whereas the calcalkalic magmas formed by melting shallower, more rigid lithospheric mantle that had been modified previously by additions of melts and fluids over the 40 Ma lifetime of the arc. The presence of more refractory olivine and spinel compositions in primitive calcalkalic basalts supports the notion that they are derived from distinct sources (Smith and Leeman, 2005).

More evolved andesitic to dacitic and even rhyolitic rocks comprise significant volumes in most volcanic arcs, particularly those sited on relatively mature continental margins (cf. Leeman, 1983). Origins of these magmas are undoubtedly varied. They may be derivative from more mafic magmas, represent partial melts of local crust, or be produced by some combination of these processes. Ongoing debate on this topic is motivated by interest in using magma chemistry to understand physical and chemical processes in subduction zones, their potential contributions to crustal formation or

1141 modification, and the effects of subduction on recycling of evolved materials to the
1142 deeper mantle. For example, if primary arc magmas are predominantly basaltic, then net
1143 removal of a mafic to ultramafic component from such material is required to produce the
1144 inferred 'andesitic' composition of average continental crust (cf. Kay and Kay, 1993; Lee
1145 et al., 2006).

1146 Alternatively, the occurrence of high Mg-number (Mg# = molar 100*Mg/[Mg+Fe])
1147 andesitic (or 'HMA') lavas in some arcs suggests the possibility that significant volumes
1148 of arc crust may be derived directly from the mantle (Kelemen et al., 2003; Tatsumi,
1149 2006; Straub et al., 2011). It has also been proposed that some HMA magmas could be
1150 melting products of subducted basaltic oceanic crust (Kay, 1978; Yogodzinski et al.
1151 2015), particularly if subduction zone temperatures are sufficiently high (e.g., where
1152 young lithosphere is being subducted or tectonic conditions favor advective heating; e.g.,
1153 Defant and Drummond, 1990; Yogodzinski et al., 2001). The latter scenario predicts
1154 melting of eclogitic rocks under conditions such that the melts would attain distinctive
1155 garnet-dominated chemical signatures (notably, MORB-like or primitive radiogenic
1156 isotopic compositions, enrichment of LREE and elevated Sr/Y, La/Yb, etc. – so-called
1157 'adakitic' signatures; Drummond and Defant, 1990; Martin et al., 2005; Moyen, 2009;
1158 Zellmer, 2009). The occurrence of such lavas has been documented in many arcs
1159 (Yogodzinski and Kelemen, 1998; Kelemen et al., 2003; Danyushevsky et al., 2008; cf.
1160 Wood and Turner, 2009), including rare examples in the Cascades (Anderson, 1974;
1161 Grove et al., 2002).

1162 However, the importance of such magmas to crustal growth is uncertain for the
1163 following reasons. First, the occurrence of significant volumes of basaltic lavas in
1164 virtually all intraoceanic arcs (Gill, 1981; Leeman, 1983) implies that these are the
1165 dominant product of mantle melting, whereas HMA magmas are subordinate in volume
1166 in most arcs. This appears to be the case for the Cascade arc. Moreover, Tolstykh et al.
1167 (2017) document the rarity of adakitic melt inclusions in adakitic (HMA-like) rocks
1168 worldwide. Second, HMA-type rocks occur in a variety of geologic settings (incl.
1169 greenstone belts, collision zones, etc.) other than active arcs, which suggests that they
1170 may be produced in multiple ways (cf. Richards and Kerrick, 2007; Moyen, 2009; Qian
1171 and Hermann, 2013). Third, many HMA-type magmas bear evidence of a hybrid origin

(e.g., Tatsumi et al., 2006; Rodriguez et al., 2007; Qian and Hermann, 2010; Straub et al., 2011), in which case it is unclear to what extent they represent primary magmas.

ACKNOWLEDGEMENTS

We are especially grateful to Arnaud Agranier, John Chesley and Cin-Ty Lee for support both with analytical work and for helpful discussions during the course of this investigation. We thank Chris Heinrich for facilitating access to the LA-ICP-MS facility within the Mineral Resource group at ETH and Marcel Guillong for his analytical expertise and help with the laser analyses. Tim Grove kindly provided a split of sample 85-41b for comparative analysis. We also benefitted from communications with Fred Anderson, Ilya Bindeman, Tim Grove, Peter Kelemen, Marion Le Voyer, Dan Ruscitto, Paul Wallace, and many others. We note that Dan Ruscitto and Paul Wallace shared unpublished data on B contents of their melt inclusions. Finally, we thank M. Rowe and S. DeBari for very useful reviews of the paper, and S. Straub for being a sympathetic editor. This work was partly supported by National Science Foundation grants EAR00-03612 and EAR04-09423 to WPL and by grant EAR03-37556 to MJS.

REFERENCES CITED

Anderson, A.T. (1974) Evidence for a picritic, volatile-rich magma, beneath Mt. Shasta, California. Journal of Petrology, 15, 243-267.

Allen, C.M., and Barnes, C.G. (2006) Ages and some cryptic sources of Mesozoic plutonic rocks in the Klamath Mountains, California and Oregon. In A.W. Snoke, and C.G. Barnes, Eds., Geological studies in the Klamath Mountains province, California and Oregon: A volume in honor of William P. Irwin: Geological Society of America Special Paper 410, 1-29, doi: 10.1130/2006.2410.11.

Bacon, C.R. and Druitt, T.H. (1988) Compositional evolution of the zoned calcalkaline magma chamber of Mount Mazama, Crater Lake, Oregon. Contributions to Mineralogy and Petrology, 98, 224-256.

Bacon, C.R., Bruggman, P.E., Christiansen, R.I., Clynne, M.A., Donnelly-Nolan, J.M. and Hildreth, W. (1997) Primitive magmas at five Cascade volcanic fields: Melts from hot, heterogeneous sub-arc mantle. The Canadian Mineralogist 35, 397-423.

Baggerman, T.D., and DeBari, S.M. (2011) The generation of a diverse suite of Late Pleistocene and Holocene basalt through dacite lavas from the northern Cascade arc at Mount Baker, Washington. Contributions to Mineralogy and Petrology, 161, 75-99.

Baker M.B., Grove T.L. and Price R. (1994) Primitive basalts and andesites from the Mt. Shasta region, N. California: products of varying melt fraction and water content. Contributions to Mineralogy and Petrology 118, 111-129.

Barr J., Grove T.L. and Elkins-Tanton L.T. (2007) High-magnesian andesite from Mount Shasta: A product of magma mixing and contamination, not a primitive melt: comment and reply. Geology doi: 10.1130/G24058C.1, e147.

Barr, J.A., Grove, T.L., and Carlson, R.W. (2008) Primitive subduction zone magmatism at Mt. Shasta, California: Geochemical and Petrologic characteristics of hydrous mantle derived melts. Eos, Transactions of the American Geophysical Union, 89(53) Fall Meeting Supplement, Abstract V33C-2226.

Bindeman, I.N., Eiler, J.M., Yogodzinski, G.M., Tatsumi, Y., Stern, C.R., Grove, T.L., Portnyagin, M., Hoërnle, K., and Danushevsky, L.V. (2005) Oxygen isotope evidence for slab melting in modern and ancient subduction zones. Earth and Planetary Science Letters, 235, 480-496.

Blondes, M.S., Brandon, M.T., Reiners, P.W., Page, F.Z., and Kita, N.T. (2012) Generation of forsteritic olivine ($Fo_{99.8}$) by subsolidus oxidation in basalt flows. Journal of Petrology, 53, 971-984.

Borg, L.E., and Clynne, M.A. (1998) The petrogenesis of felsic calc-alkaline magmas from the southernmost Cascades, California: Origin by partial melting of basaltic lower crust. Journal of Petrology, 39, 1197-1222.

Borg, L.E., Clynne, M.A. and Bullen, T.D. (1997) The variable role of slab-derived fluids in the generation of a suite of primitive calc-alkaline lavas from the southernmost Cascades, California. The Canadian Mineralogist, 35, 425-452.

1231 Borg, L. E., Blichert-Toft, J. and Clynne, M. A. (2002) Ancient and modern subduction
1232 zone contributions to the mantle sources of lavas from the Lassen region of California
1233 inferred from Lu-Hf isotopic systematics. Journal of Petrology, 43, 705-723.

1234 Brophy, J.G. (2008) A study of rare earth element (REE)-SiO_2 variations in felsic liquids
1235 generated by basalt fractionation and amphibolite melting: A potential test for
1236 discriminating between the two. Contributions to Mineralogy and Petrology, 156, 337–
1237 357.

1238 Brophy, J.G., Whittington, C.S. and Park, Y.-R. (1999) Sector-zoned augite megacrysts
1239 in Aleutian high alumina basalts: Implications for the conditions of basalt
1240 crystallization and the generation of calc-alkaline series magmas. Contributions to
1241 Mineralogy and Petrology, 135, 277-290.

1242 Cashman K.V. (1993) Relationship between plagioclase crystallization and cooling rate
1243 in basaltic melts. Contributions to Mineralogy and Petrology, 113:126–142.

1244 Ceuleneer, G. and Le Sueur, E. (2008) The Trinity Ophiolite (California): The strange
1245 association of fertile mantle peridotite with ultra-depleted crustal cumulates. Bulletin
1246 de Societe Geologique Francaise, 179, 503-518.

1247 Christiansen, R.L., Kleinhampl, F.J., Blakely, R.J., Tuchek, E.T., Johnson, F.L., and
1248 Conyac, M.D. (1977) Resource appraisal of the Mt. Shasta wilderness study area,
1249 Siskiyou County, California. Open-file Report 77–250, U.S. Geol. Survey, 53 pp.

1250 Clynne, M.A. (1999) A complex magma mixing origin for rocks erupted in 1915, Lassen
1251 Peak, California. Journal of Petrology, 40, 105-132.

1252 Conrey, R.M., Sherrod, D.R., Hooper, P.R. and Swanson, D.A. (1997) Diverse primitive
1253 magmas in the Cascade arc, northern Oregon and southern Washington. The
1254 Canadian Mineralogist, 35, 367-396.

1255 Cortes, J.A., Wilson, M., Condliffe, E. and Francalanci, L. (2006) The occurrence of
1256 forsterite and highly oxidizing conditions in basaltic lavas from Stromboli Volcano,
1257 Italy. Journal of Petrology, 47, 1345-1373.

1258 Costa F., Dohmen R., Chakraborty S. (2008) Time scales of magmatic processes from
1259 modeling the zoning patterns of crystals. Reviews in Mineralogy and Geochemistry,
1260 69, Mineralogical Society of America, Washington, D.C., 545–594.

Danyushevsky, L.V., Falloon, T.J., Crawford, A.J., Tetroeva, S.A. and Leslie, R.L., and Verbeeten, A. (2008) High-Mg adakites from Kadavu Island Group, Fiji, southwest Pacific: Evidence for the mantle origin of adakite parental melts. Geology, 36, 499-502.

DeBari, S.M., Anderson, R.G., and Mortensen, J.K. (1999) Correlation among lower to upper crustal components in an island arc: The Jurassic Bonanza arc, Vancouver Island, Canada. Canadian Journal of Earth Science, 36, 1371-1413.

Defant, M.J., and Drummond M.S. (1990) Derivation of some modern arc magmas by melting of young subducted lithosphere. Nature, 347, 662-665.

Drummond, M.S., and Defant, M.J. (1990) A model for trondjhemite-tonalite-dacite genesis and crustal growth via slab melting. Journal of Geophysical Research, 95, 21503-21521.

Evans, B.W. (1977) Metamorphism of alpine peridotite and serpentinite. Annual Reviews in Earth Science, 5, 397-447.

Evans, B.W., (2008) Control of the products of serpentinization by the $Fe^{2+}Mg_{-1}$ exchange potential of olivine and orthopyroxene. Journal of Petrology, 49, 1873-1887.

Feeley, T.C., Clynne, M.A., Winer, G.S., and Grice, W.C. (2008) Oxygen isotope geochemistry of the Lassen Volcanic Center, California: Resolving crustal and mantle contributions to continental arc magmatism. Journal of Petrology, 49, 971-997.

Galer, S.J.G., and Abouchami, W. (1998) Practical application of lead triple spiking for correction of instrumental mass discrimination. Mineralogical Magazine, 62A, 491-492.

Gao, P., Zheng, Y.-F., and Zhao, Z.-F. (2016) Experimental meltx from crustal rocks: A lithochemical constraint on granite petrogenesis. Lithos, 266-267, 133-157.

Garrido, C.J., Sánchez-Vizcaíno, V.L, Gómez-Pugnaire, M.T., Trommsdorff, V., Alard, O., Bodinier, J.L. and Godard, M. (2005) Enrichment of HFSE in chlorite-harzburgite produced by high-pressure dehydration of antigorite-serpentinite: Implications for subduction magmatism. Geochemistry Geophysics and Geosystems 6, Q01J15, doi:10.1029/2004GC000791.

George R., Turner S., Hawkesworth C.J., Bacon C.R., Nye C., Stelling P. and Dreher S. (2004) Chemical versus temporal controls on the evolution of tholeiitic and calc-alkaline magmas at two volcanoes. Journal of Petrology, 45, 203-219.

Gill, J.B. (1981) Orogenic Andesites and Plate Tectonics. Springer-Verlag, 390 pp.

Greene, A.R., DeBari, S.M., Kelemen, P.K., Blusztajn, J., and Clift, P.D. (2006) A detailed geochemical study of island arc crust: The Talkeetna Arc section, south-central Alaska. Journal of Petrology, 47, 1051-1093.

Green, N.L. (2006) Influence of slab thermal structure on basalt source regions and melting conditions: REE and HFSE constraints from the Garibaldi volcanic belt, northern Cascadia subduction system. Lithos, 87, 23-49.

Green, N.L. and Sinha, A.K. (2005) Consequences of varied slab age and thermal structure on enrichment processes and melting regimes in the sub-arc mantle of the northern Cascadia subduction system. Journal of Volcanology and Geothermal Research, 140, 107-132, doi:10.1016/j.jvolgeores.2004.07.017.

Grove, T.L., Parman, S.W., Bowring, S.A., Price, R.C. and Baker, M.B. (2002) The role of H_2O-rich fluid component in the generation of primitive basaltic andesites and andesites from the Mt. Shasta region, N California. Contributions to Mineralogy and Petrology, 142, 375-396.

Grove, T.L., Elkins-Tanton, L.T., Parman, S.W., Chatterjee, N., Müntener, O. and Gaetani, G.A. (2003) Fractional crystallization and mantle-melting controls on calc-alkaline differentiation trends. Contributions to Mineralogy and Petrology, 145, 515-533.

Grove, T.L., Baker, M.B., Price, R.C., Parman, S.W., Elkins-Tanton, L.T., Chatterjee, N. and Müntener, O. (2005) Magnesian andesite and dacite lavas from Mt. Shasta, northern California: Products of fractional crystallization of H_2O-rich mantle melts. Contributions to Mineralogy and Petrology, 148, 542-565.

Gruau, G., Bernard-Griffiths, J., and Lécuyer, C. (1998) The origin of U-shaped rare earth patterns in ophiolitic peridotites: Assessing the role of secondary alteration and melt/rock ratio. Geochimica et Cosmochimica Acta, 62, 3545-3560.

1319 Harry, D.L. and Green, N.L. (1999) Slab dehydration and basalt petrogenesis in
1320 subduction systems involving very young oceanic lithosphere. Chemical Geology,
1321 160, 309-333.

1322 Herrmann, W., and Berry, R.F. (2002) MINSQ – a least squares spreadsheet method for
1323 calculating mineral proportions from whole rock major element analyses.
1324 Geochemistry: Exploration, Environment, Analysis, 2, 361–368.

1325 Horodyskyj, U., Lee, C.-T.A. and Luffi, P. (2009) Geochemical evidence for exhumation
1326 of eclogite via serpentinite channels in ocean-continent subduction zones. Geosphere,
1327 5, 426-438.

1328 Humphreys, M.C.S., Edmonds, M., Plail, M., Barclay, J., Parkes, D., and Christopher, T.
1329 (2013) A new method to quantify the real supply of mafic components to a hybrid
1330 andesite. Contributions to Mineralogy and Petrology, 165, 191-215.

1331 Jacobsen, S.B., Quick, J.E., and Wasserburg, G.J. (1984) A Nd and Sr isotopic study of
1332 the Trinity peridotite: Implications for mantle evolution. Earth and Planetary Science
1333 Letters, 68, 361-378.

1334 Kay R. W. (1978) Aleutian magnesian andesites: Melts from subducted Pacific ocean
1335 crust. Journal of Volcanology and Geothermal Research, 4, 117–132.

1336 Kay, R.W. and Kay, S.M. (1993) Delamination and delamination magmatism.
1337 Tectonophysics, 219, 177-189.

1338 Kelemen, P.B., Hanghoj, K. and Greene, A.R. (2003) One view of the geochemistry of
1339 subduction-related magmatic arcs, with an emphasis on primitive andesite and lower
1340 crust. Treatise of Geochemistry, 3, 593-659.

1341 Kelemen P.B. and Yogodzinski G. (2007) High-magnesian andesite from Mount Shasta:
1342 A product of magma mixing and contamination, not a primitive melt: Comment and
1343 reply. Geology, 35, doi: 10.1130/G24099C.1

1344 Kodolányi, J., and Pettke, T. (2011) Loss of trace elements from serpentinites during
1345 fluid-assisted transformation of chrysotile to antigorite – An example from Guatemala.
1346 Chemical Geology, 284, 351-362.

1347 LaPierre, H., Brouxel, M., Albaréde, F., Coulon, C., Lécuyer, C., Martin, P., Mascle, G.,
1348 and Rouer, O. (1987) Paleozoic and lower Mesozoic magmas from the eastern

1349 Klamath Mountains (North California) and the geodynamic evolution of northwestern
1350 America. Tectonophysics, 140, 155-177.

1351 Lecuyer, C., and Fourcade, S. (1991) Oxygen isotope evidence for multi-stage
1352 hydrothermal alteration at a fossil slow-spreading center: The Silurian Trinity
1353 Ophiolite (California, U.S.A.). Chemical Geology, 87, 231-246.

1354 Lee, C.-T.A., Cheng, X. and Horodyskyj, U. (2006) The development and refinement of
1355 continental arcs by primary basaltic magmatism, garnet pyroxenite accumulation,
1356 basaltic recharge and delamination: Insights from the Sierra Nevada, California.
1357 Contributions to Mineralogy and Petrology, 151, 222-242, doi:10.1007/s00410-005-
1358 0056-1.

1359 Lee, C.-T.A., Harbert, A., and Leeman, W.P. (2007) Extension of lattice strain theory to
1360 mineral/mineral rare-earth element partitioning: An approach for assessing
1361 disequilibrium and developing internally consistent partition coefficients between
1362 olivine, orthopyroxene, clinopyroxene and basaltic melt. Geochimica et
1363 Cosmochimica Acta, 71, 481-496.

1364 Lee, C.-T.A., Luffi, P., Plank, T., Dalton, H., and Leeman, W.P. (2009) Constraints on
1365 the depths and temperatures of basaltic magma generation on Earth and other
1366 terrestrial planets using new thermobarometers for mafic magmas. Earth and Planetary
1367 Science Letters, 279, 20-33.

1368 Leeman, W.P. (1983) The influence of crustal structure on compositions of subduction-
1369 related magmas. Journal of Volcanology and Geothermal Research, 18, 561-588.

1370 Leeman, W.P., Smith, D.R., Hildreth, W., Palacz, Z.A. and Rogers, N.W. (1990)
1371 Compositional diversity of late Cenozoic basaltic magmas of the southern Washington
1372 Cascades. Journal of Geophysical Research, 95, 19561-19582.

1373 Leeman, W.P., Lewis, J.F., Evarts, R.C., Conrey, R.M. and Streck, M.A. (2005)
1374 Petrologic constraints on the thermal structure of the Cascades arc. Journal of
1375 Volcanology and Geothermal Research, 140, 67-105, doi:10.1016/
1376 j.jvolgeores.2004.07.016.

Le Voyer, M., Rose-Koga, E.F., Shimizu, N., Grove, T.L. and Schiano, P. (2010) Two contrasting H_2O-rich components in primary melt inclusions from Mount Shasta. Journal of Petrology, 51, 1571-1595.

Lofgren G. (1980) Experimental studies on the dynamic crystallization of silicate melts, In R.B. Hargraves, Ed., Physics of Magmatic Processes, Princeton University Press, 478-551.

López, S., Castro, A., and Garcia-Casco, A. (2005) Production of granodiorite melt by interaction between hydrous mafic magma and tonalitic crust: Experimental constraints and implications for the generation of Archean TTG complexes. Lithos, 79, 229-250.

Magna, T., Wiechert, U., Grove, T.L., and Halliday, A.N. (2006) Lithium isotope fractionation in the southern Cascadia subduction zone. Earth and Planetary Science Letters, 250, 428-443.

Martin, E., Bindeman, I. and Grove, T.L. (2011) The origin of high-Mg magmas in Mt. Shasta and Medicine Lake volcanoes, Cascade Arc (California): Higher and lower than mantle oxygen isotope signatures attributed to current and past subduction. Contributions to Mineralogy and Petrology, 162, 945-960.

Martin, H., Smithies, R.H., Rapp, R., Moyen, J.-F., and Champion, D. (2005) An overview of adakite, tonalite-trondhjemite-granodiorite (TTG) and sanukitoid: Relationships and some implications for crustal evolution. Lithos, 79, 1-24.

Mitchell, A.L., and Grove, T.L. (2015) Melting the hydrous subarc mantle: The origin of primitive andesites. Contributions to Mineralogy and Petrology, 170:13, doi:10.1007/s00410-015-1161-4.

Moyen, J.F. (2009) High Sr/Y and La/Yb ratios: The meaning of the "adakitic signature". Lithos, 112, 556-574.

Müntener, O, Kelemen, P.B. and Grove, T.L. (2001) The role of H_2O during crystallization of primitive arc magmas under the uppermost mantle conditions and genesis of igneous pyroxenites: An experimental study. Contributions to Mineralogy and Petrology, 141, 643-658.

1406 Nakagawa, M., Wada, K., and Wood, P. (2002) Mixed magmas, mush chambers and
1407 eruption triggers: Evidence from zones clinopyroxene phenocrysts in andesitic scoria
1408 from the 1995 eruptions of Ruapehu volcano, New Zealand. Journal of Petrology, 43,
1409 2279-2303.

1410 Newman, S., Macdougall, J.D. and Finkel, R.C. (1986) Petrogenesis and ^{230}Th–^{238}U
1411 disequilibrium at Mt. Shasta, California, and in the Cascades. Contributions to
1412 Mineralogy and Petrology, 93, 195–206.

1413 Pedrón-Navarta, J.A., Hermann, J., Garrido, C.J., Sánchez-Vizcaíno, V.L, and Gómez-
1414 Pugnaire, M.T. (2010) An experimental investigation of antigorite dehydration in
1415 natural silica-enriched serpentinite. Contributions to Mineralogy and Petrology, 159,
1416 25-42.

1417 Pichavant, M., Mysen, B.O., and Macdonald, R. (2002) Source and H_2O content of high-
1418 MgO magmas in island arc settings: An experimental study of a primitive calc-
1419 alkaline basalt from St. Vincent, Lesser Antilles arc. Geochimica et Cosmochimica
1420 Acta, 66, 2193-2209.

1421 Putirka, K.D. (2008) Thermometers and barometers for volcanic systems. Reviews in
1422 Mineralogy and Geochemistry, 69, Mineralogical Society of America, Washington,
1423 D.C., 61-120.

1424 Qian, Q. and Hermann, J. (2010) Formation of high-Mg diorites through assimilation of
1425 peridotite by monzodiorite magma at crustal depths. Journal of Petrology, 51, 1381-
1426 1416.

1427 Qian, Q., and Hermann, J. (2013) Partial melting of lower crust at 10-15 kbar:
1428 Constraints on adakite and TTG formation. Contributions to Mineralogy and
1429 Petrology, 165, 1195-1224.

1430 Quick, J.E. (1981) Petrology and petrogenesis of the Trinity peridotite, an upper mantle
1431 diapir in the eastern Klamath Mountains, Northern California. Journal of Geophysical
1432 Research, 86, 11837-11863.

1433 Reiners, P.W., Hammond, P.E., McKenna, J.M. and Duncan, R.A. (2000) Young basalts
1434 of the central Washington Cascades, flux melting of the mantle, and trace element

signatures of primary arc magmas. Contributions to Mineralogy and Petrology, 138, 249-264.

Richards, J.P. and Kerrick, R. (2007) Adakite-like rocks: Their diverse origins and questionable role in metallogenesis. Economic Geology, 102, 537-576.

Righter, K. (2000) A comparison of basaltic volcanism in the Cascades and western Mexico: Compositional diversity in continental arcs. Tectonophysics, 318, 99-117.

Rodriguez, C., Selles, D., Dungan, M.A., Langmuir, C.H. and Leeman, W.P. (2007) Adakitic dacites formed by intracrustal crystal fractionation of water-rich parent magmas at Nevado de Longaví volcano (36.2°S; Andean Southern Volcanic Zone, central Chile)., Journal of Petrology 48, 2033-2061. doi:10.1093/petrology/egm049.

Rowe, M.C., Kent, A.J.R. and Nielsen, R.L. (2009) Subduction influence on oxygen fugacity and trace and volatile elements in basalts across the Cascade volcanic arc. Journal of Petrology, 50, 61-91.

Ruscitto, D.M., Wallace, P.J. and Kent, A.J.R. (2011) Revisiting the compositions and volatile contents of olivine-hosted melt inclusions from the Mount Shasta region: Implications for the formation of high-Mg andesites. Contributions to Mineralogy and Petrology, 162, 109-132. doi:10.1007/s00410-010-0587-y.

Sas, M., DeBari, S.M., Clynne, M.A., and Rusk, B.G. (2017) Using mineral chemistry to decipher slab, mantle, and crustal input in the generation of high-Mg andesites and basaltic andesites from the northern Cascade Arc. American Mineralogist, 102, 948-965.

Scambelluri, M., Bottazzi, P., Trommsdorff, V., Vannucci, R., Hermann, J., Gómez-Pugnaire, M.T. and Sánchez-Vizcaíno, V.L (2001) Incompatible element-rich fluids released by antigorite breakdown in deeply subducted mantle. Earth and Planetary Science Letters, 192, 457-470.

Schiano, P., Monzier, M., Eissen, J.-P., Martin, H. and Koga, K.T. (2010) Simple mixing as the major control of the evolution of volcanic suites in the Ecuadorian Andes. Contributions to Mineralogy and Petrology, 160, 297-312.

1463 Schwindinger, K.R., and Anderson, A.T. (1987) Probable low-pressure intrusion of
1464 gabbro into serpentinized peridotite, northern California. Geological Society of
1465 America Bulletin, 98, 364-372.

1466 Severs, M.J., Beard, J.S., Fedele, L., Hanchar, J.M., Mutchler, S.R. and Bodnar, R.J.
1467 (2009) Partitioning behavior of trace elements between dacitic melt and plagioclase,
1468 orthopyroxene, and clinopyroxene based on laser ablation ICPMS analysis of silicate
1469 melt inclusions. Geochimica et Cosmochimica Acta, 73, 2123-2141.

1470 Sisson, T.W. and Grove, T.L. (1993) Experimental investigations of the role of H_2O in
1471 calc-alkaline differentiation and subduction zone magmatism. Contributions to
1472 Mineralogy and Petrology, 113, 143-166.

1473 Sisson, T.W., Ratajeski, K., Hankins, W.B. and Glazner, A.F. (2005) Voluminous
1474 granitic magmas from common basaltic sources. Contributions to Mineralogy and
1475 Petrology, 148, 635-661.

1476 Sisson, T.W., Salters, V.J.M., and Larson, P.B. (2014) Petrogenesis of Mount Rainier
1477 andesite: Magma flux and geologic controls on the contrasting differentiation styles at
1478 stratovolcanoes of the southern Washington Cascades. Geological Society of America
1479 Bulletin, 126, 122-144, doi:10.1130/B30852.1.

1480 Skulski, T., Minarik, W., and Watson, E.B. (1994) High-pressure experimental trace-
1481 element partitioning between clinopyroxene and basaltic melts. Chemical Geology,
1482 117, 127-147.

1483 Smith, D.R. and Leeman, W.P. (1987) Petrogenesis of Mount St. Helens dacitic magmas.
1484 Journal of Geophysical Research, 92, 10313-10334.

1485 Smith, D.R. and Leeman, W.P. (1993) The origin of Mount St. Helens andesites. Journal
1486 of Volcanology and Geothermal Research, 55, 271–303.

1487 Smith, D.R. and Leeman, W.P. (2005) Chromian spinel-olivine phase chemistry and the
1488 origin of primitive basalts of the southern Washington Cascades. Journal of
1489 Volcanology and Geothermal Research, 140, 49-66.

1490 Snoke, A.W., and Barnes, C.G. (2006) The development of tectonic concepts for the
1491 Klamath Mountains province, California and Oregon. In A.W. Snoke, and C.G.
1492 Barnes, Eds., Geological studies in the Klamath Mountains province, California and

1493 Oregon: A volume in honor of William P. Irwin: Geological Society of America
1494 Special Paper 410, 1-29, doi: 10.1130/2006.2410(11).

1495 Sobolev, A.V., Hofmann, A.W., Sobolev, S.V., and Nikogosian, I.K. (2005) An olivine-
1496 free mantle source of Hawaiian shield basalts. Nature, 434, 590-597,
1497 doi:10.1038/nature03411.

1498 Stone, W.E., Fleet, M.E. and MacRae, N.D. (1989) Two-phase nickeliferous monosulfide
1499 solid solution (mss) in megacrysts from Mount Shasta, California: A natural laboratory
1500 for nickel-copper sulfides. American Mineralogist, 74, 981-993.

1501 Straub, S.M., Gomez-Tuena, A., Stuart, F.M., Zellmer, G.F., Espinasa-Perena, R., Cai, Y.
1502 and Iizuka, Y. (2011) Formation of hybrid arc andesites beneath thick continental
1503 crust. Earth and Planetary Science Letters, 303, 337-347.

1504 Streck, M.J. (2008) Mineral textures and zoning as evidence for open system processes.
1505 In: Minerals, Inclusions, and Volcanic Processes, Reviews of Mineralogy and
1506 Geochemistry 69, Mineralogical Society of America, Washington, D.C., 595-619.

1507 Streck, M.J., Leeman, W.P. and Chesley, J.S. (2007a) High magnesian andesite from
1508 Mount Shasta: A product of magma mixing and contamination, not a primitive mantle
1509 melt. Geology, 35, 351-354.

1510 Streck, M.J., Leeman, W.P. and Chesley, J.S. (2007b) High magnesian andesite from
1511 Mount Shasta: A product of magma mixing and contamination, not a primitive mantle
1512 melt: Reply 2. Geology, 35, doi: 10.1130/G24356Y.1.

1513 Streck, M.J., Leeman, W.P., and Chesley, J.S. (2007c) High magnesian andesite from
1514 Mount Shasta: A product of magma mixing and contamination, not a primitive mantle
1515 melt: Reply 1. Geology, 35, doi: 10.1130/G24177Y.1.

1516 Tatsumi, Y. (2006) High-Mg andesites in the Setouchi volcanic belt, SW Japan: Analogy
1517 to Archean magmatism and continental crust formation? Annual Reviews of Earth and
1518 Planetary Sciences 34, 467-499.

1519 Tatsumi, Y., Kawabata, H., Sato, K., Miyazaki, T., Chang, Q., Takahashi, T., Tani, K.,
1520 Shibata, T. and Yoshikawa, M. (2006) The petrology and geochemistry of Oto-Zan
1521 composite lava flow on Shodo-Shima Island, SW Japan: Remelting of a solidified
1522 high-Mg andesite magma. Journal of Petrology, 47, 595-629.

Thibodeau, A.M., Killick, D.J., Ruiz, J., Chesley, J.T., Deagan, K., Cruxent, J.M., and Lyman, W. (2007) The strange case of the earliest silver extraction by European colonists in the New World. Proceedings of the National Academy of Science, 104, 3363-3366, doi:10.1073/pnas.0607297104.

Thibodeau, A.M., Killick, D.J., Hedquist, S.L., Chesley, J.T., and Ruiz, J. (2015) Isotopic evidence for the provenance of turquoise in the southwestern United States. Geological Society of America Bulletin, 127, 1617-1631.

Tiepolo, M., Tribuzio, R., and Langone, A. (2011) High-Mg andesite petrogenesis by amphibole crystallization and ultramafic crust assimilation: Evidence from Adamello hornblendites (Central Alps, Italy). Journal of Petrology, 52, 1011-1045.

Tiepolo, M., Langone, A., Morishita, T., and Yuhara, M. (2012) On the recycling of amphibole-rich ultramafic intrusive rocks in the arc crust: Evidence from Shikanoshima Island (Kyushu, Japan). Journal of Petrology, 53, 1255-1285.

Tolstykh, M.L., Naumov, V.B., and Yarmolyak, V.V. (2017) Adakites and adakitic melts: Compositions of rocks, quenched glasses, and inclusions in minerals. Petrology, 25, 304-317.

Turner, S., Hawkesworth, C., Rogers, N., Bartlett, J., Worthington, T., Hergt, J., Pearce, J., and Smith, I. (1997) ^{238}U-^{230}Th disequilibria, magma petrogenesis, and flux rates beneath the depleted Tonga-Kermadec island arc. Geochimica et Cosmochimica Acta, 61, 4855-4884.

Vance, J.A. and Dungan, M.A. (1977) Formation of peridotites by deserpentinization in the Darrington and Sultan areas, Cascade Mountains, Washington. Geological Society of America Bulletin, 88, 1497-1508.

Volpe, A.M. (1992) ^{238}U–^{230}Th–^{226}Ra disequilibria in young Mt. Shasta andesites and dacites. Journal of Volcanology and Geothermal Research, 53, 227-238.

Walowski, K.L., Wallace, P.J., Hauri, E.H., Wada, I., and Clynne, M.A. (2015) Slab melting beneath the Cascade arc driven by dehydration of altered oceanic peridotite. Nature Geoscience, 8, 404-408.

1551 Walowski, K.J., Wallace, P.J., Clynne, M.A., Rasmussen, D.J., and Weis, D. (2016) Slab
1552 melting and magma formation beneath the southern Cascade arc. Earh Planet. Sci.
1553 Lett., 446, 100-112.
1554 Whitaker, M.L., Nekvasil, H., Lindsley, D.H. and McCurry, M. (2008) Can
1555 crystallization of olivine tholeiite give rise to potassic rhyolites? – An experimental
1556 investigation. Bulletin of Volcanology, 70, 417-434.
1557 Wood, B.J. and Turner, S.P. (2009) Origin of primitive high-Mg andesite: Constraints
1558 from natural examples and experiments. Earth and Planetary Science Letters, 283, 59-
1559 66.
1560 Yogodzinski, G.M. and Kelemen, P.B. (1998) Slab melting in the Aleutians: Implications
1561 of an ion probe study of clinopyroxene in primitive adakite and basalt. Earth and
1562 Planetary Science Letters, 158, 53-65.
1563 Yogodzinski, G.M., Lees, J.M., Churikova, T.G., Dorendorf, F., Woërner, G. and
1564 Volynets, O.N. (2001) Geochemical evidence for the melting of subducting oceanic
1565 lithosphere at plate edges. Nature, 409, 500-504.
1566 Yogodzinski, G.M., Brown, S.T., Kelemen, P.B., Vervoort, J.D., Portnyagin, M., Sims,
1567 K.W.W., Hoërnle, K., Jicha, B.R., and Werner, R. (2015) The role of subducted basalt
1568 in the source of island arc magmas: Evidence from seafloor lavas of the western
1569 Aleutians. Journal of Petrology, 56, 441-492.
1570 Yu, X., and Lee, C.-T.A. (2016) Critical porosity of melt segregation during crustal
1571 melting: Constraints from zonation of peritectic garnets in a dacite volcano. Earth and
1572 Planetary Science Letters, 449, 127-134.
1573 Zellmer, G.F. (2009) Petrogenesis of Sr-rich adakitic rocks at volcanic arcs: Insights from
1574 global variations of eruptive style with plate convergence rates and surface heat flux.
1575 Journal of the Geological Society of London, 166, 725-734.
1576 Zellmer, G.F., Annen, C., Charlier, B.L.A., George, R.M.M., Turner, S.P., and
1577 Hawkesworth, C.J. (2005) Magma evolution and ascent at volcanic arcs: Constraining
1578 petrogenetic processes through rates and chronologies. Journal of Volcanology and
1579 Geothermal Research, 140, 171-191.
1580

1581 **FIGURES**

1582

1583 Fig. 1: Harker diagrams for Shasta lavas showing SiO_2 vs. [a] MgO, [b] CaO, [c] Al_2O_3,
1584 and [d] Na_2O (all in wt.%). Plots for K_2O, FeO*, and TiO_2 (not shown) also define near-
1585 linear arrays (labeled 'mixing' in panel [a]) for the lavas (data from Grove et al., 2002).
1586 Samples are distinguished as basaltic, andesitic, dacitic, and high-Mg andesite (HMA)
1587 lavas; also plotted are groundmass ('GM', this study) and average 'HMA-' and 'PBA-
1588 type' melt inclusions (annotated 'R" for average of Ruscitto et al. (2011) and 'PBA for
1589 our average; cf. Table 2), and average melt inclusions ('LV') from several Shasta basaltic
1590 lavas (Le Voyer et al., 2010). Yellow field shows loci of experimental liquids produced
1591 from primitive mafic lavas (Sisson and Grove, 1993; Müntener et al., 2001; Pichavant et
1592 al., 2002; Grove et al., 2002, 2003; Sisson et al., 2005; Whitaker et al., 2008). Heavy
1593 arrowed curves show fractional crystallization trends for water-bearing liquids produced
1594 from a Shasta basaltic andesite (85-44; blue, FCb) and the Shasta HMA (85-41b; black,
1595 FCa) at pressures between 0.8 and 1.2 GPa; at lower pressures, plagioclase occurs as a
1596 near-liquidus phase, causing depletion of Al_2O_3 (effect shown in panel [c] for
1597 experiments conducted at 1.2 vs. 0.2 GPa). Also shown are fields for experimental melts
1598 of mafic amphibolites distinguished by pressure of the experiments (data taken from
1599 review by Gao et al., 2016). These are screened to exclude mica-bearing starting
1600 compositions (that tend to produce granitic melts). At pressures below ~1.5 GPa (gray
1601 field), plagioclase is a residual phase, whereas above 1.5 GPa (red-outlined open field)
1602 garnet is present, and these minerals strongly influence the Al_2O_3 and Na_2O contents of
1603 partial melts; in [a] the two sets of experiments overlap and are not distinguished.

1604

1605 Fig. 2: Oblique Google Earth view of Mt. Shasta and the adjacent Whaleback shield
1606 volcano from a northeast perspective. Red cross indicates locality of samples described
1607 in this paper. Inset map shows general location of this area.

1608

1609 Fig. 3: (a) West side of Whaleback Quarry, showing locations (dots or vertical bar) of
1610 analyzed samples in the context of the exposed stratigraphy; (b) hand sample of MS-16-
1611 04 showing olivine-rich xenolithic fragments; (c) MgO vs. SiO_2 for all Whaleback

Quarry samples; (d) Cr vs. MgO, showing the up-section increase in these components. All samples of the pyroclastic layers are volcanic bombs except for MS-13-04, MS-14-04 that are tephra samples used by Ruscitto et al. (2011); these two samples are not plotted as there are no bulk compositional data for tephra samples.

Fig. 4: (a) Al and (b) Cr vs. Mg# in analyzed HMA pyroxenes. Lowest Mg# (59) of one orthopyroxene (opx) plots offscale. Low Mg# compositions (<80) are found in cores of Type 1 pyroxene phenocrysts while highest Mg# (>88) are typically found in rims of phenocrysts. Range of typical Type 1 pyroxene compositions shown by solid bar for rims and open bar for crystal cores. Resorbed opx crystals have compositions clustering around Mg# 87 (cf. Figs 5, 6, 7 and see text).

Fig. 5: BSE images of representative Type 1 (antecrystic) pyroxenes; note that lowermost grain in panel (d) is a Type 3 pyroxene. Each phenocryst is labeled to indicate crystal type (opx vs. cpx). White dots show loci of individual analyses; adjacent numbers are Mg#. White lines within crystals in panels (b) and (d) indicate loci of the analytical traverses shown in inset. Black empty areas in opx crystal of (a) are artifacts of sample preparation. Scale bar is 200 μm in all panels.

Fig. 6: Analytical traverses across two Type 1 clinopyroxene crystals at point spacing of ~1.5 μm. From right to left, traverses start within low Mg# core portion and end at the rim. Importantly, step profiles across low to high Mg# domains are similar for both faster (Fe, Mg) and slower (Cr) diffusing cations; also, approaching the rims, Cr sharply decreases (albeit not as low as the core compoitions) whereas Mg# drops less dramatically (only to 82-84). These two profiles were used to calculate relaxation times for diffusion; optimal fits suggest times on the order of a few months (see text).

Fig. 7: Transmitted light (a, inset of d) and BSE images (b, c, d) of Type 2 pyroxenes. High Mg# core of Type 2 pyroxene is characterized by strong resorption channels leading to coarsely spongy texture and by patchy zoning with occasionally distinct overgrowth of low Mg# pyroxene (b, d). In many cases, complex and mostly xenocrystic core is

overgrown by high Mg# euhedral rim (b, c, and partly d). Type 3 clinopyroxenes are present in upper center of panel (b) and upper left of panel (c);-the latter has an opx core overgrown by cpx and is adjacent to an opx microlite (dark gray shade) with Mg# ~90. Inset in (d) is a transmitted light image of same grain. Scale bar is 200 μm in each panel; dots show analysis loci with Mg#.

Fig. 8: Transmitted light (a, c) and BSE images (b, d) of Type 1 (xenocrystic) olivines. (a) shows micro-crystalline (mostly opx) reaction selvage inside and around olivine; (b) shows lighter reaction fringe of Fo_{87} olivine on more magnesian crystal; no overgrowth is is observed along the top and lower right edges of the crystal, juxtaposing Fo_{93} olivine against groundmass that crystallized ~Fo_{88-85} olivine; (c) anhedral Fo_{93} relic olivine core jacketed by euhedral Fo_{88} olivine; (d) remnant of requilibrated Fo_{93} olivine overgrown by Fo_{86} olivine. Scale bar is 200 μm in each panel. Dots indicate analysis loci with Fo content; in (b) are shown compositions along analysis traverse.

Fig. 9: Images of other olivine variants. (a) BSE image of skeletal Type 2 olivine; (b) transmitted light image of skeletal but nearly euhedral Type 2 olivine; this texture is consistent with rapid crystal growth or quenching; (c, d) transmitted light images of two Type 3 olivine clusters with cumulate-like textures; these are both single lapilli extracted from tephra samples MS-13-04 and MS-14-04. Intergrain and surrounding material are opx veins described in text and seen in Fig 11b. Dots indicate analysis loci with Fo content.

Fig. 10: Fo vs. NiO compositions of olivine crystals (xls) of different types. Type 2 (phenocrystic) and Type 3 (micro-xenocrystic) olivines are shown in Fig. 9.. Type 1 olivines are part of ‘single crystals’ and compositional spread of crystal interiors is indicated by bracket. Compositions of Type 1 olivine fall into fields of mantle peridotites except those with less than 0.3 wt.% NiO and those higher than Fo_{93} that fall outside of the compilation by Sobolev et al. (2005) as shown by grayed field.

Fig. 11: Compositions of (a) spinels, and (b) olivine-spinel pairs. BSE image in (a) shows spinel-bearing olivine inclusion within a reacting disequilibrium orthopyroxene grain. Reflected light image in (b) shows oxide-rich opx vein in olivine micro-xenoliths of Figure 9c and 9d. Spinel variants are distinguished by symbols as follows: spinel in veins (mostly opx) of olivine micro-xenoliths (open orange triangles); spinel in olivine of micro-xenoliths (inverted open blue triangles); spinel in olivine included within the pictured Mg#84 orthopyroxene (open red cross); groundmass spinel (small open green circles) grouped by sample in which they are found. Other symbols: rare spinel in skeletal Fo_{87} olivine (filled green diamonds); rare spinel in late grown Type 3 cpx and in rim of Type 1 cpx (filled green circles); rare spinel in Fo_{93} Type 1 olivine (half-filled squares). Also shown are compositional fields for spinel of the Trinity Ophiolite (Quick, 1981) and experimental spinels (black crosses) (Grove et al., 2003).

Fig. 12: FeO* vs. mole% An compositions of plagioclases. Key: large crystals that are phenocryst-sized or glomerocrystic (L); HMA groundmass crystal (G); rare plagioclase inclusions in Mg#77 pyroxene (I); and plagioclase composition from experiments at 0.1 and 200 MPa (E; Grove et al., 2003). Composition range for plagioclase from Mt. Shasta dacites is indicated by horizontal arrow. Vertical arrows indicate predicted An contents for plagioclases hypothetically in equilibrium with indicated K_d values which increase with magmatic water content (Sisson and Grove, 1993); solid arrows with HMA composition magma and open arrows for dacitic melt inclusion (left) and of HMA groundmass (right) of Table 2. The observed plagioclase compositions preclude their formation from HMA magma under water-rich conditions.

Fig. 13: Map of crystals and vesicles in thin section of sample MS-16-04. All pyroxene crystals >70 μm in size were classified and color coded according to the textural criteria discussed in the text. Histograms show distribution of pyroxene types according to size. An interactive version of this map provides access to BSE images and compositional data for analyzed crystals can be accessed at: https://www.pdx.edu/geology/streck-

Shasta-HMA. See also Supplemental Figure A7 for high-resolution BSE image of entire thin section.

Fig. 14: (a) REE profiles for Type 1 clinopyroxene cores and rims, (b) calculated melts in equilibrium with Type 1 core compositions using D_{REE} in clinopyroxene (see text) and HMA inclusions and groundmass (Table 2, Fig. 1), and (c) representative Shasta dacite lavas (Grove et al., 2003) and whole rock HMA averages of our data and of sample 85-41b whole rock (cf. Table 1). Stippled field in (b) shows range for Shasta dacites using data of Grove et al. (2003). Note that REE profile for HMA whole rock is similar to that of Shasta dacites.

Fig. 15: Summary of phase assemblages and compositions of experiments using Mt. Shasta HMA (85-41c) as starting composition. Data are from Müntener et al. (2001) for water undersaturated experiments at P=1.2 GPa and temperatures ranging from 1230°C to 1030°C, and from Grove et al. (2003) for experiments under dry conditions at P= 0.01, water-saturated conditions at 0.2 GPa, and water-undersaturated conditions at 1.5 GPa over temperatures ranging from 1300 to 940°C.

Fig. 16: Comparative compositions of pyroxenes from experiments using Mt. Shasta HMA (#85-41c) as starting composition and naturally occurring pyroxenes of this study. Experimental data are from Müntener et al. (2001) and Grove et al. (2003); see Fig. 15 for more details.

Fig. 17: Plots showing (a) Ba vs. Sr and (b) Sr/Y vs. Sr of dacite and andesite lavas of Mt. Shasta area (Baker et al., 1994; Grove et al., 2002) and bulk, groundmass (grdm.), and melt inclusion (inc.) data for HMA (see Table 1). Arrows show effects of 50% fractional crystallization using the indicated bulk distribution coefficients (see text for discussion).

Fig. 18: Calculated incompatible trace element compositions for [a] HMA whole rock (WR) average, [b] HMA Groundmass, and [c] average HMA Melt inclusion (MI) using mixing model proportions calculated from major element data (Table 3; see text). All are normalized to the observed compositions of these materials. Multiple profiles shown in each case correspond to different assumed dacite end members (see text). Thickness of horizontal gray lines approximates analytical uncertainty on the HMA components (cf. **Tables 1 and 2**).

TABLES

Table 1. Major element, trace element, and isotopic compositions of bulk rock samples.

Table 2. Average major and trace element analyses of groundmass in sample MS-16-04. Trace elements were determined by LA-ICPMS using spot sizes of approximately 70 μm. Also included are average compositions of HMA- and PBA-type melt inclusions (data from Ruscitto et al., 2011), dacitic melt inclusions, and HMA whole-rocks from this study.

Table 3. Summary of least-squares mixing models for HMA based on major elements

Suppplemental Material

Supplement I. Isotope information

Supplement II. Melt inclusion information

Tables

A1. Pyroxenes

A2. Olivines

A3. Spinels

A4 Feldspars

A5. Cpx trace elements

A6. Supplemental compositions of Trinity Ophiolite and Shasta area lavas

A7. High resolution BSE image of entire thin section MS-16-04b.

Figures

A1. Sr-Nd-Pb isotopic variations in Shasta lavas and regional basement rocks

A2. Fo vs. liquid Mg# for Shasta MIs

A3. MgO vs. SiO_2, CaO, and FeO* in PEC-corrected Shasta MIs and representative lavas

A4. Comparison of temperature estimates for Shasta MIs

A5. P/Ti-K/Ti variations in HMA MIs and Shasta lavas

A6. Trace element variations in HMA MIs and Shasta lavas

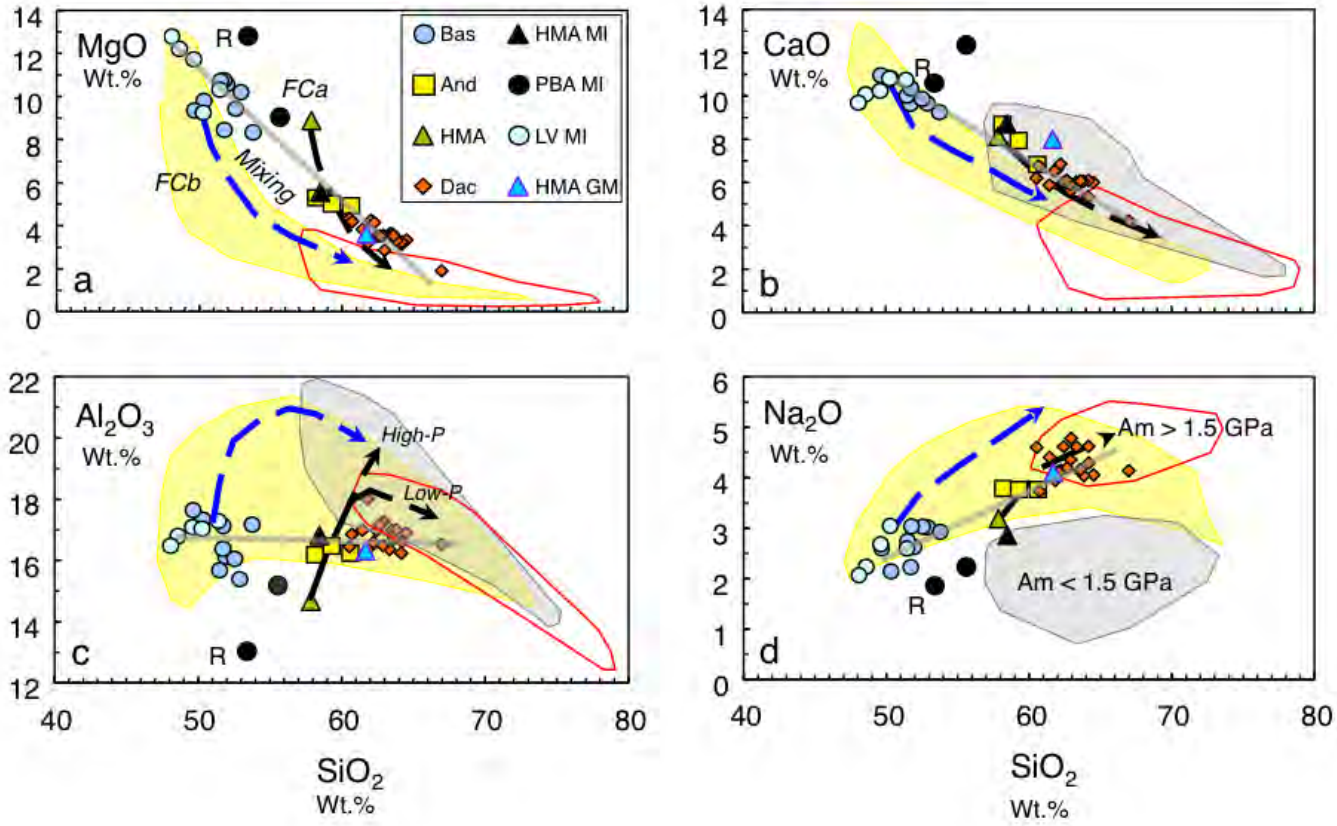
MgO
Wt.%
R
FCa
FCb
Mixing
Bas
HMA MI
And
PBA MI
HMA
LV MI
Dac
HMA GM
a
CaO
Wt.%
b
Al2O3
Wt.%
High-P
Low-P
c
Na2O
Wt.%
Am > 1.5 GPa
Am < 1.5 GPa
d
SiO2
Wt.%

Fig. 2, Streck and Leeman, Shasta HMA

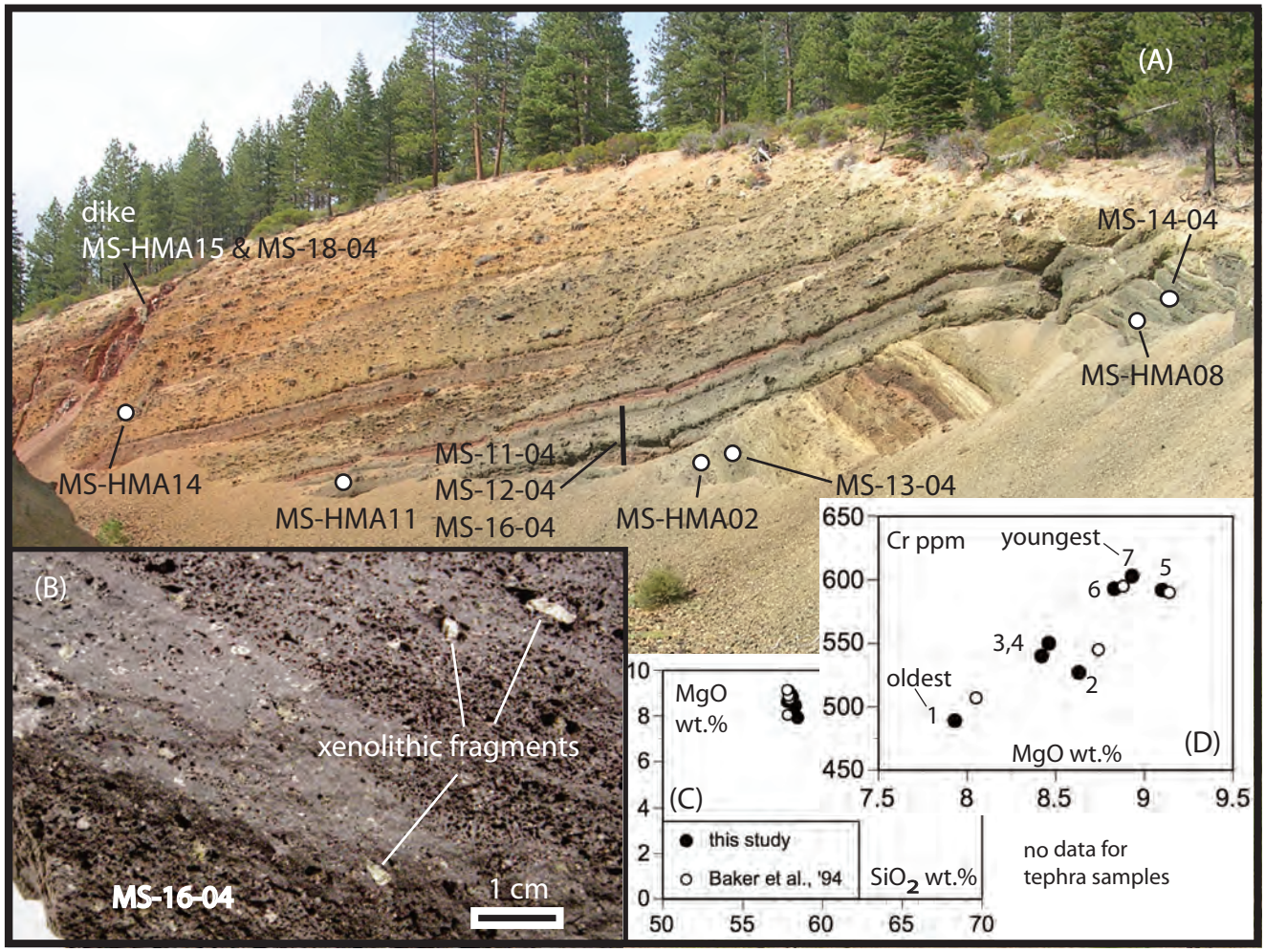

Fig. 3 Streck & Leeman_ Shasta HMA

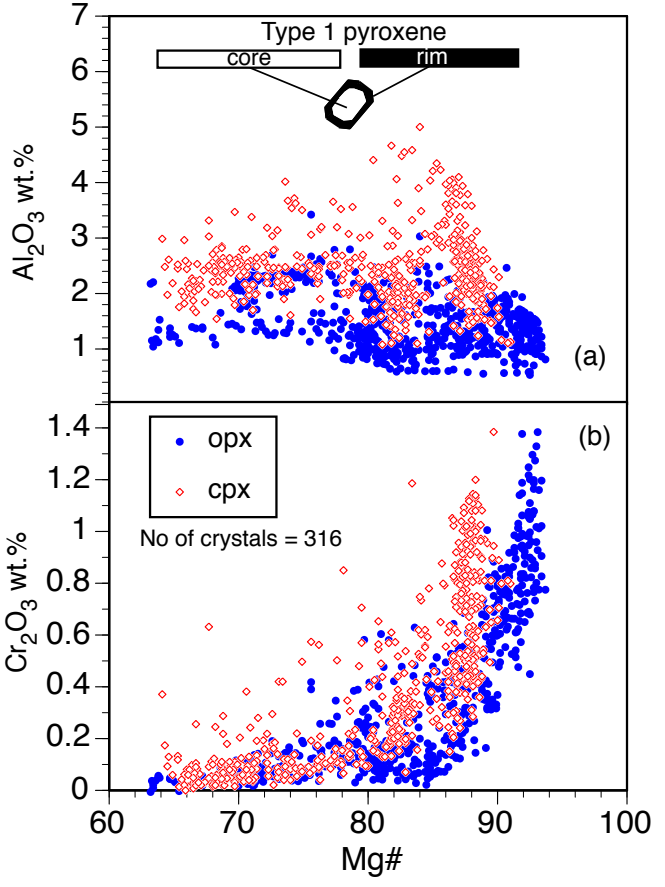

Fig. 4, Streck & Leeman, Shasta HMA

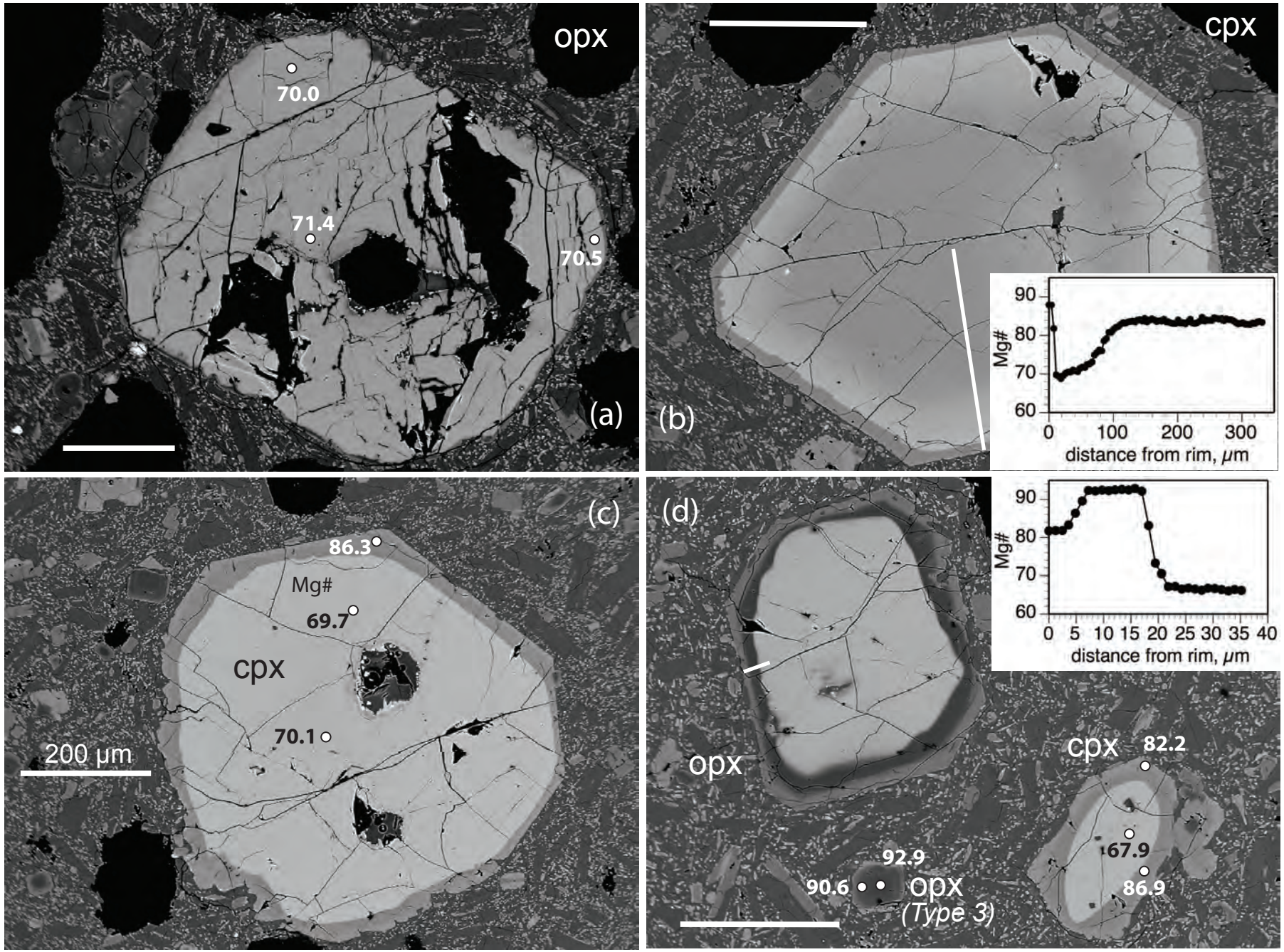

Fig. 5, Streck & Leeman, Shasta HMA

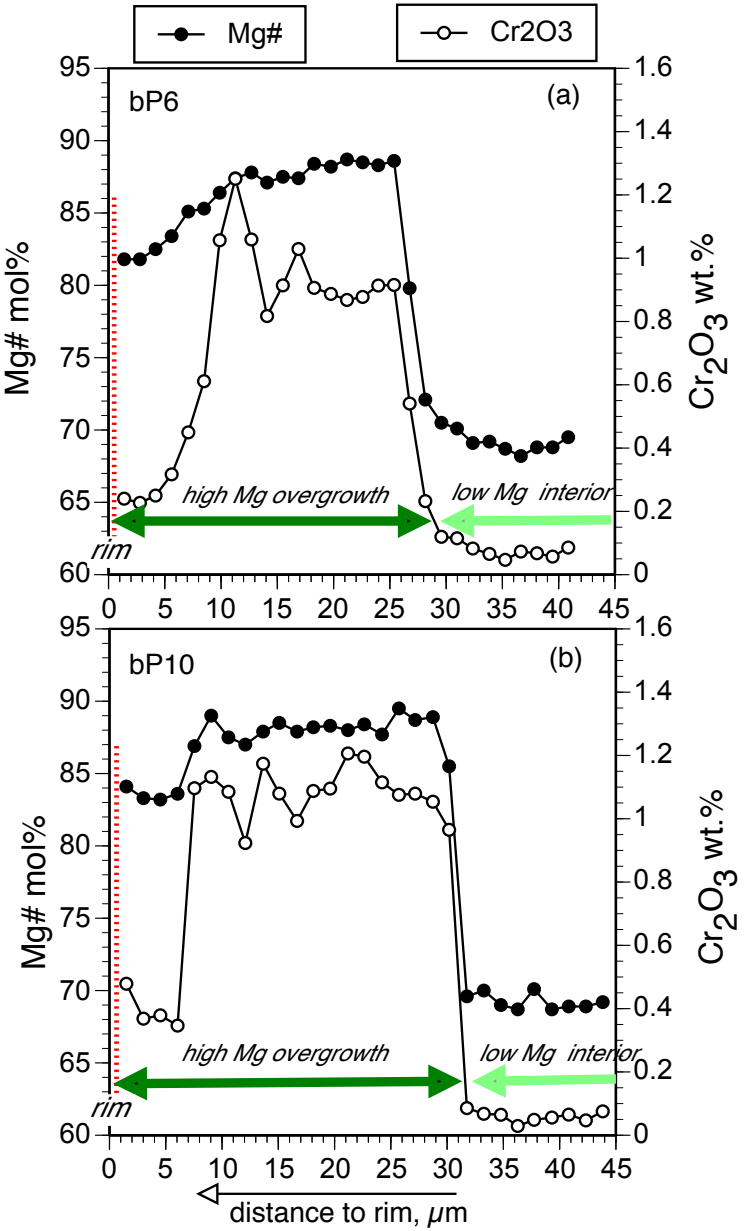

Fig. 6, Streck et al., Mt. Shasta HMA

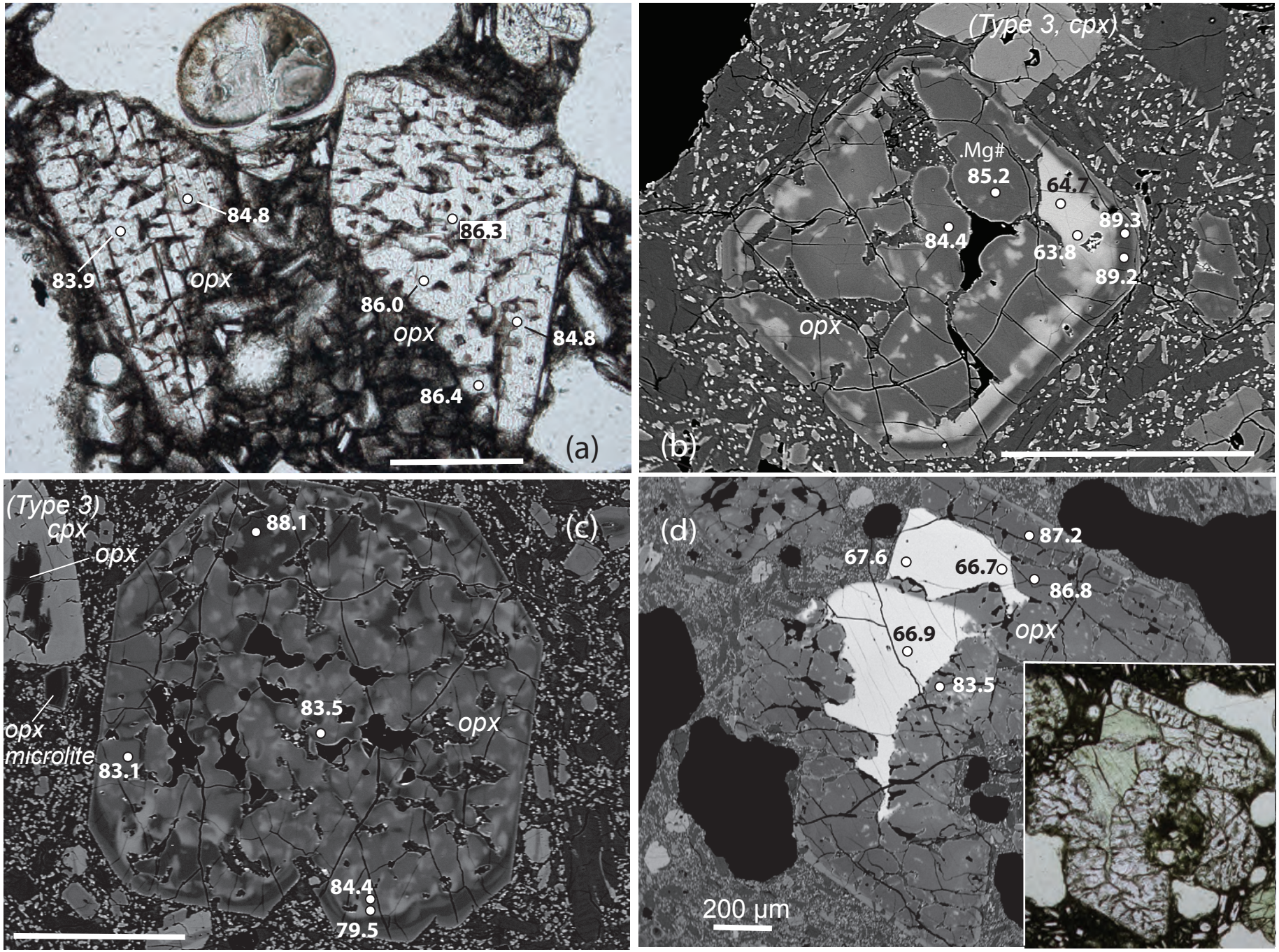

Fig. 7, Streck & Leeman, Shasta HMA

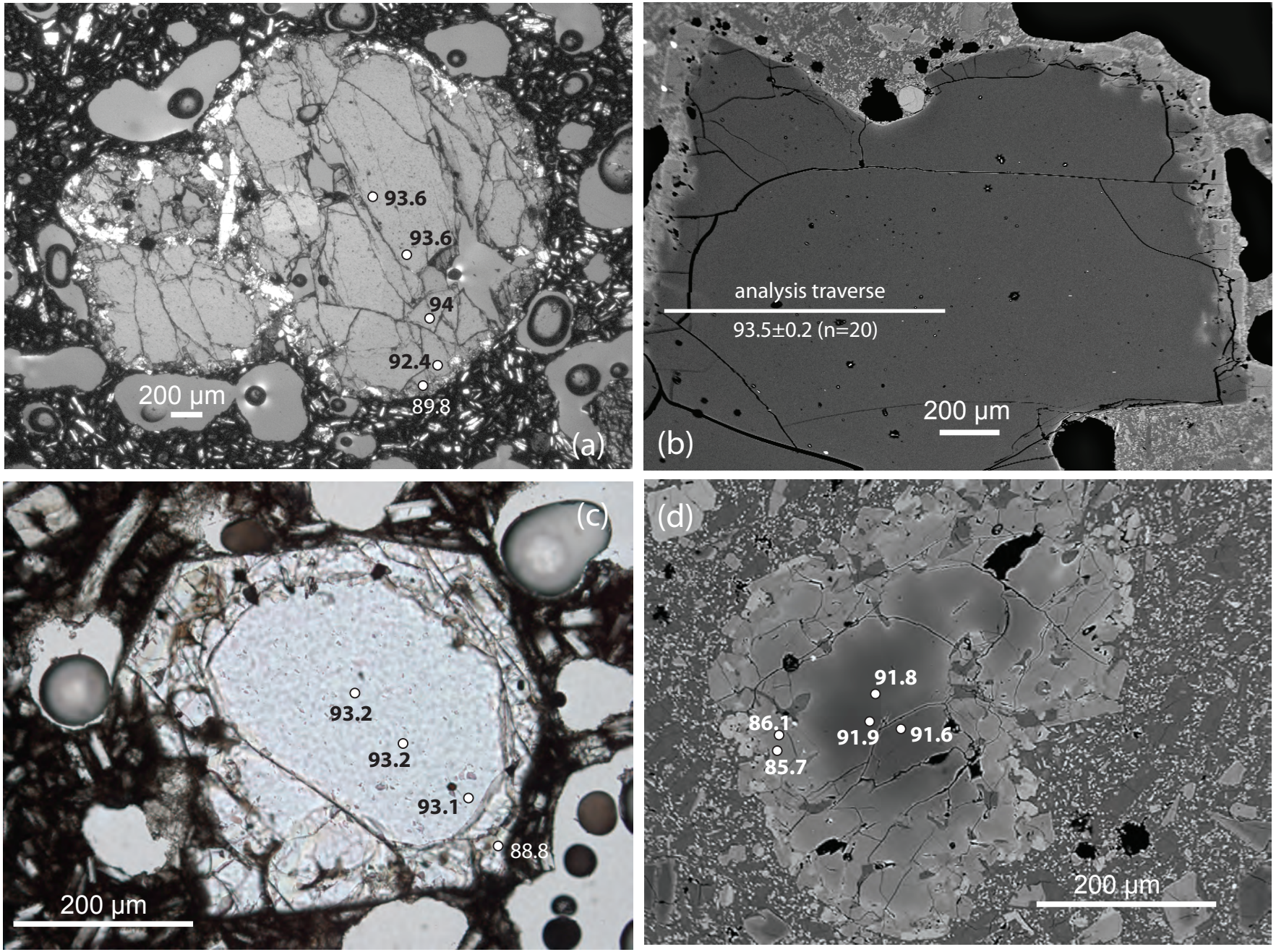

Fig. 8, Streck & Leeman, Shasta HMA

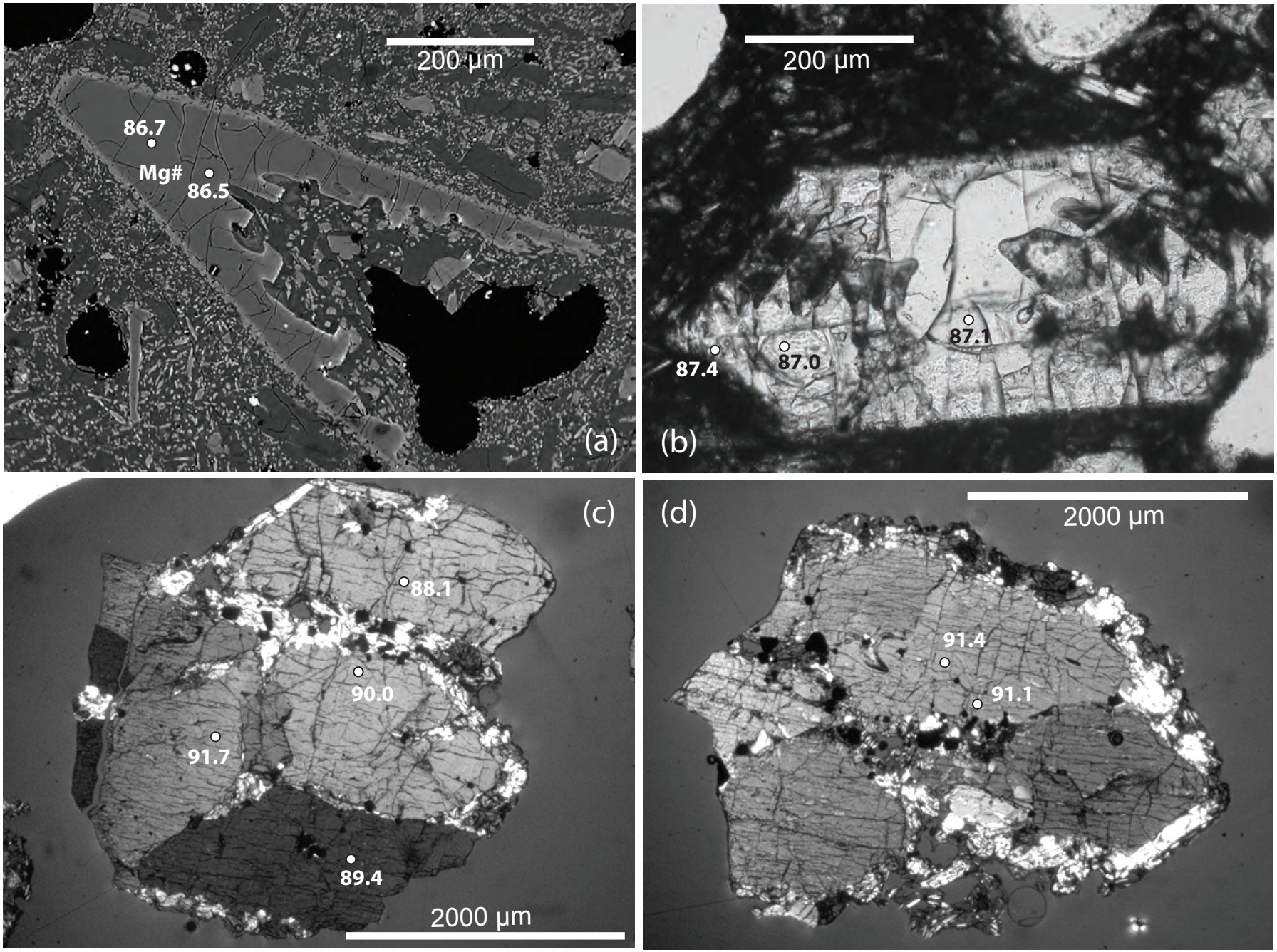

Fig. 9, Streck & Leeeman, Shasta HMA

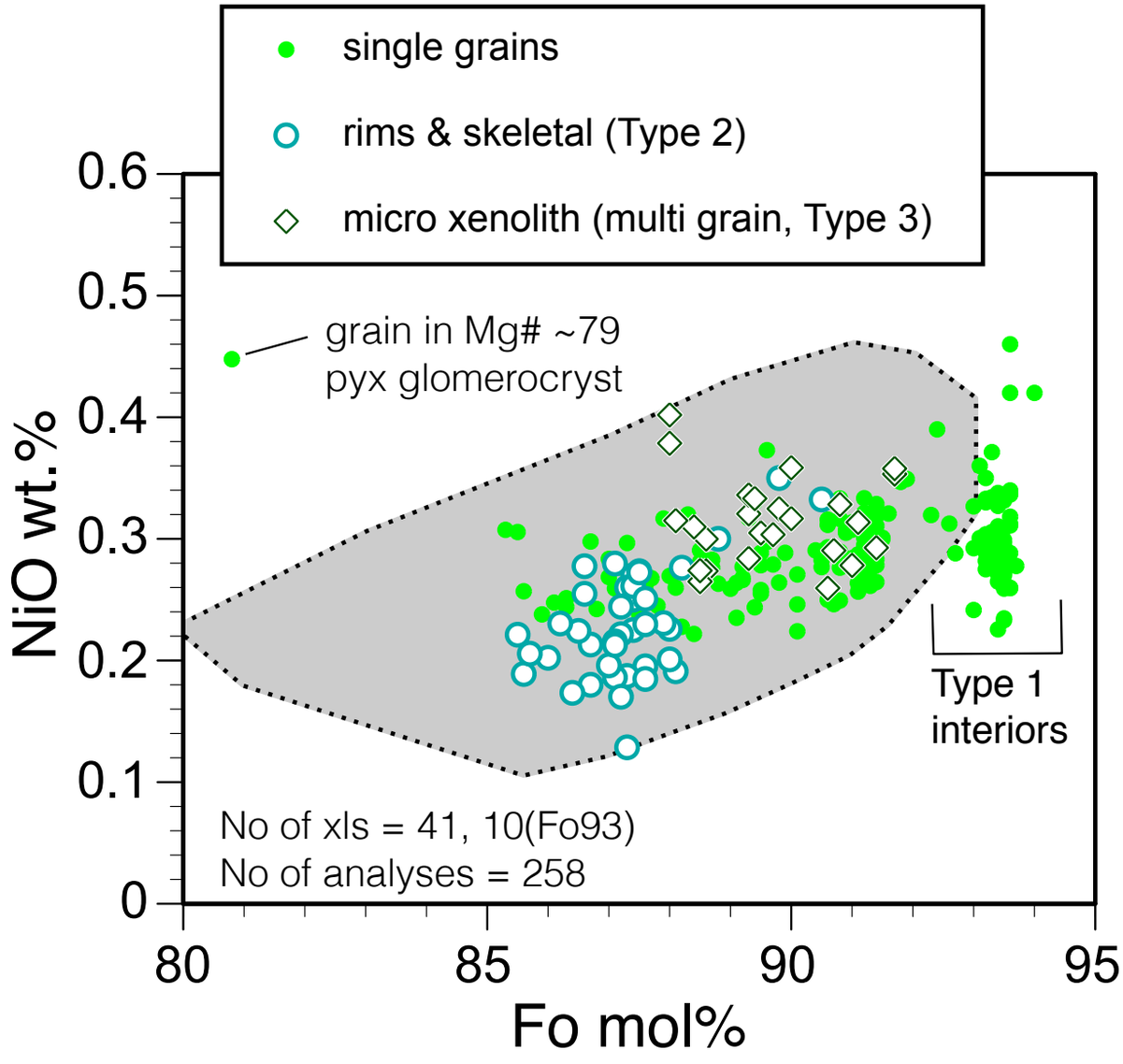

Fig. 10, Streck & Leeman, Shasta HMA

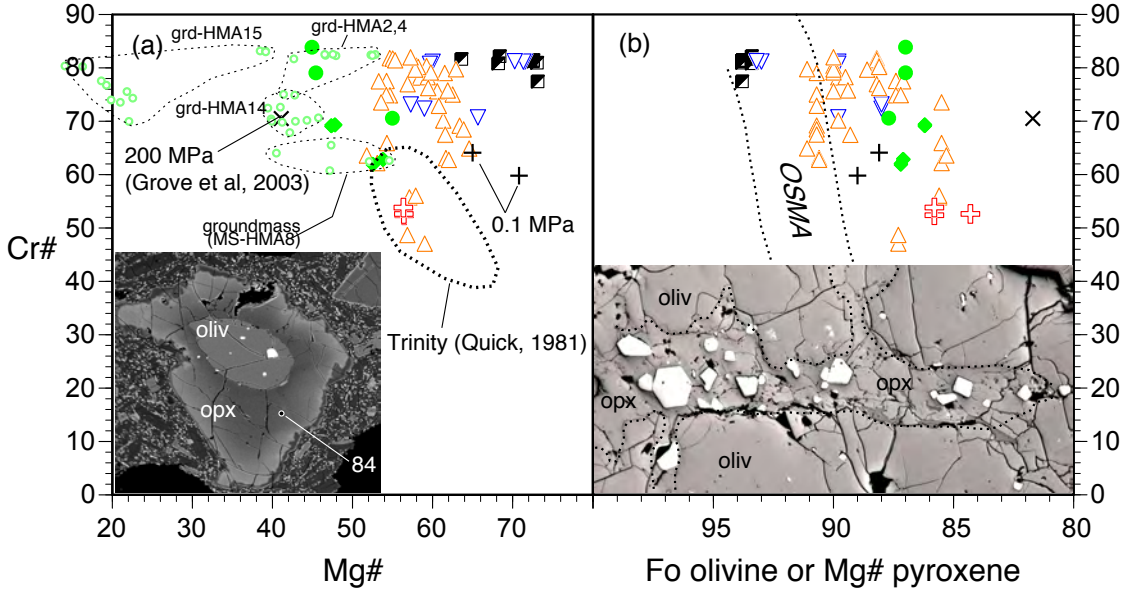

Fig. 11, Streck & Leeman, Shasta HMA

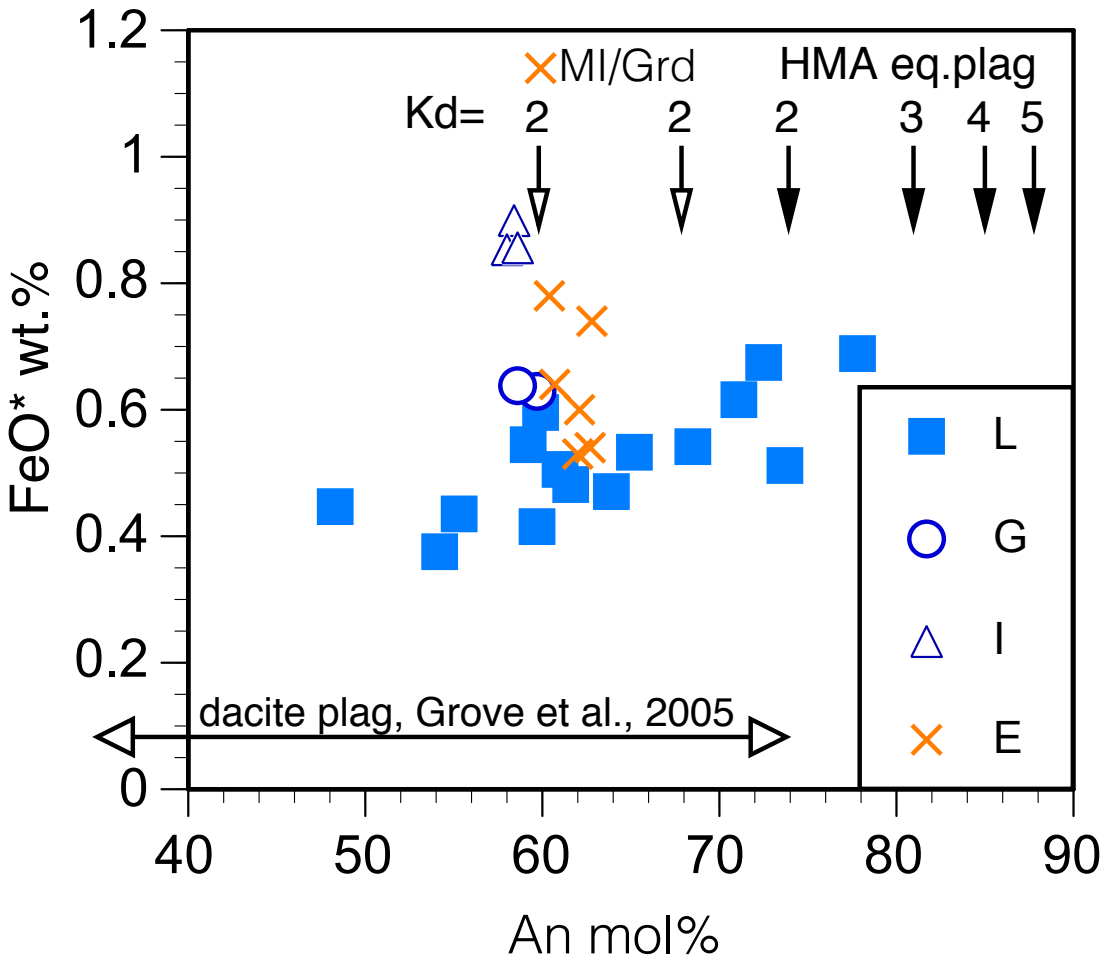

Fig. 12, Streck & Leeman, Shasta HMA

Fig. 13 Streck & Leeman, Shasta HMA

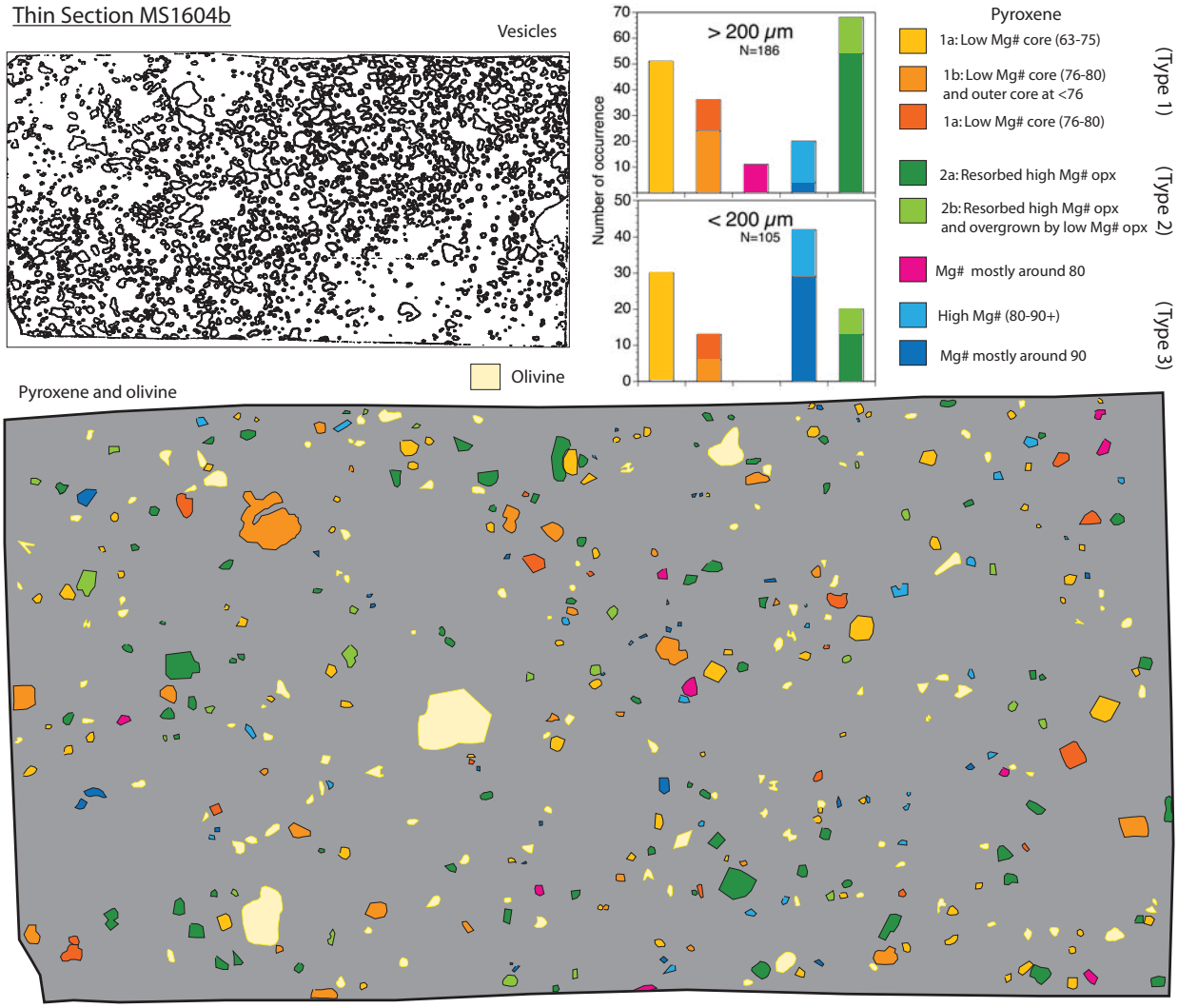

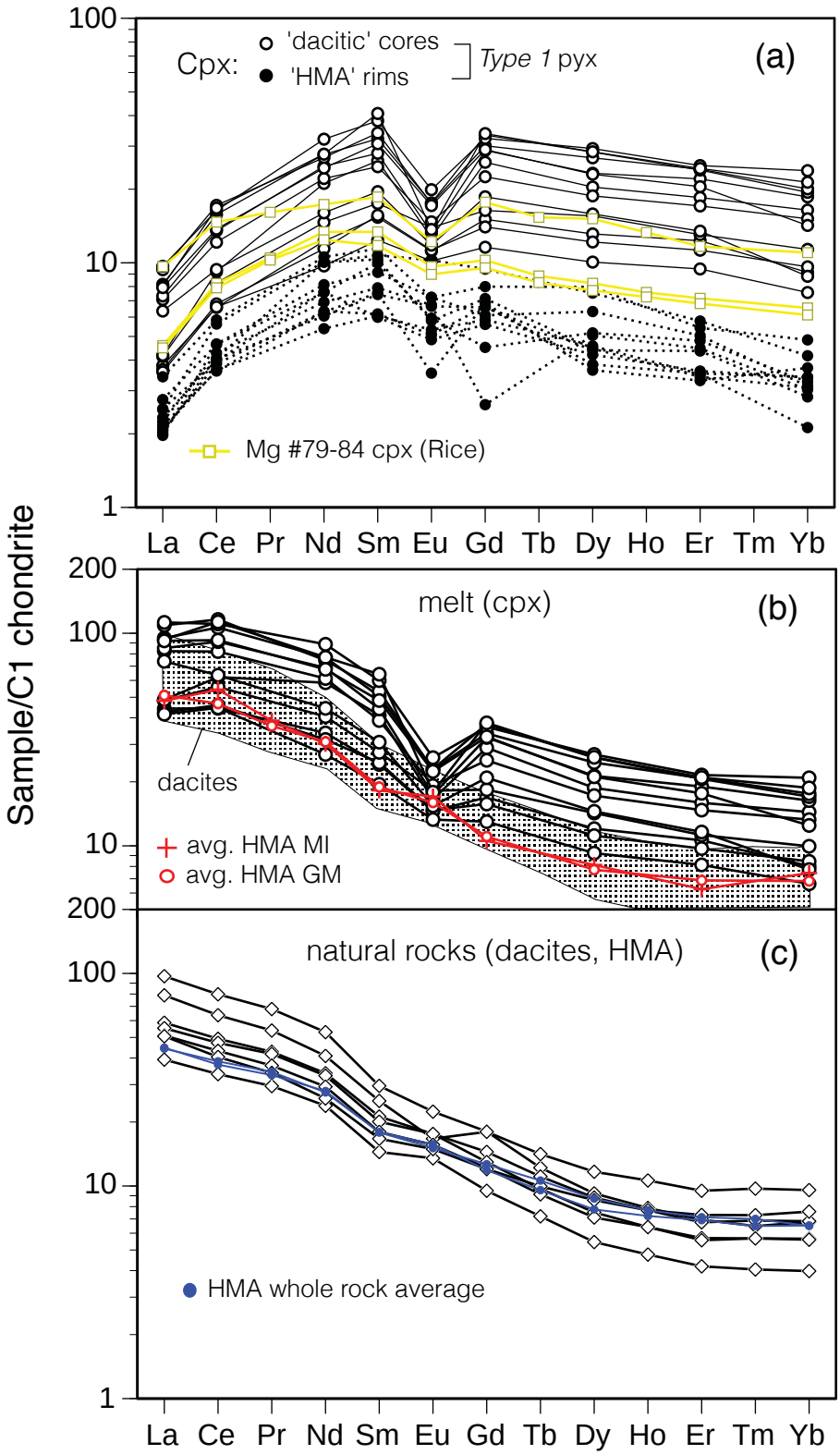

Fig.14 Streck & Leeman, Shasta HMA

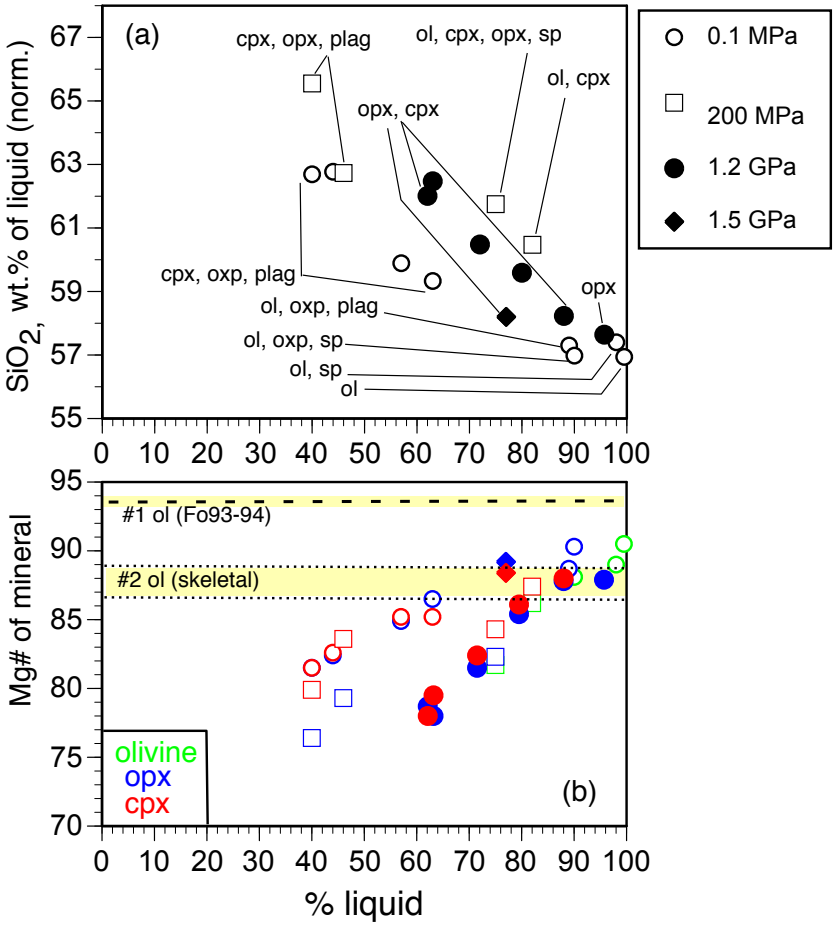

Fig.15, Streck& Leeman Shasta HMA

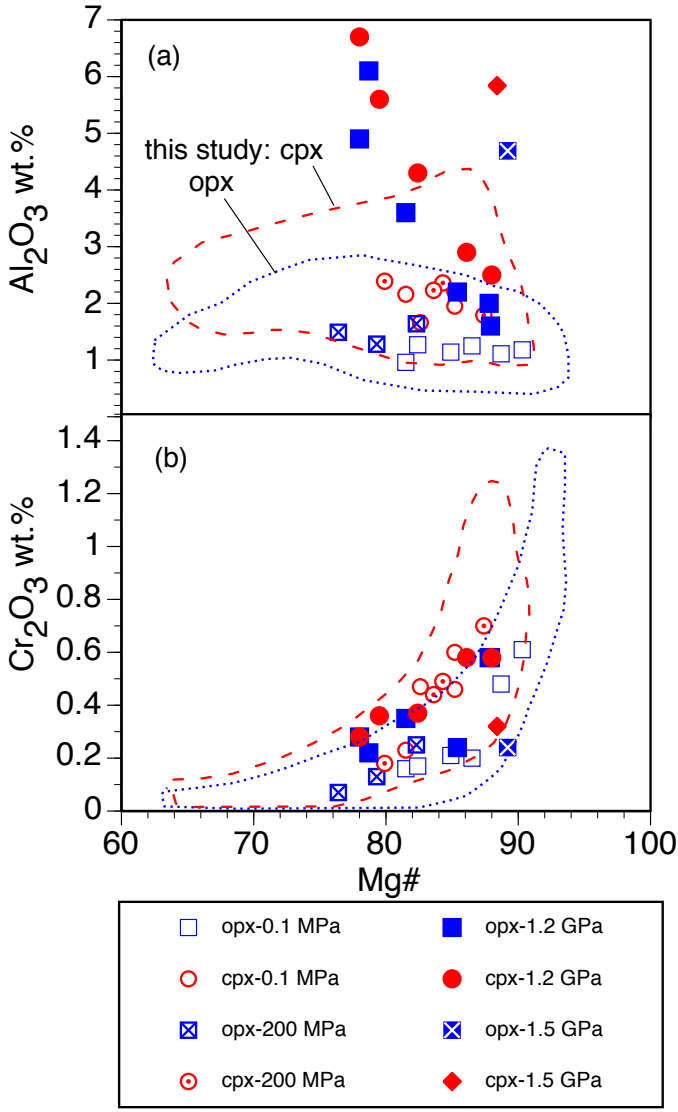

Fig. 16, Streck&Leeman, Shasta HMA

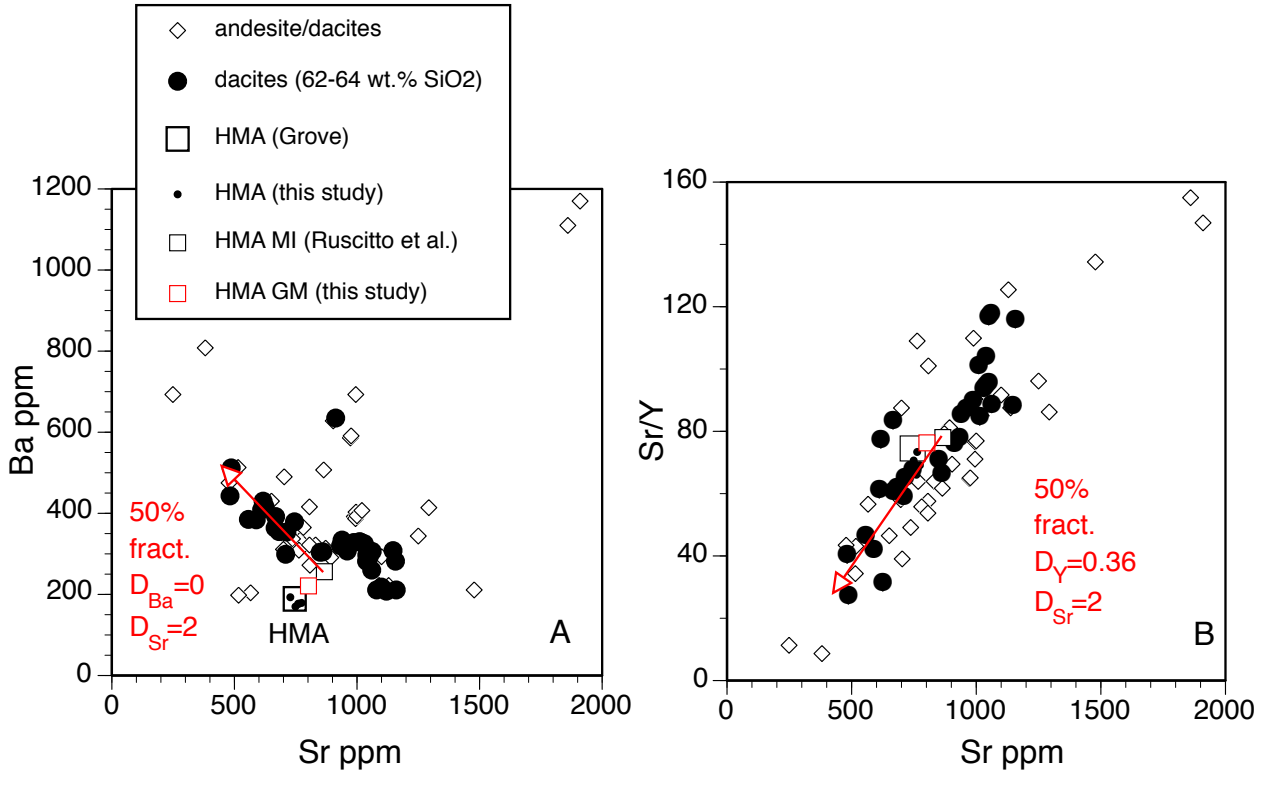

Fig. 17, Streck & Leeman, Shasta HMA

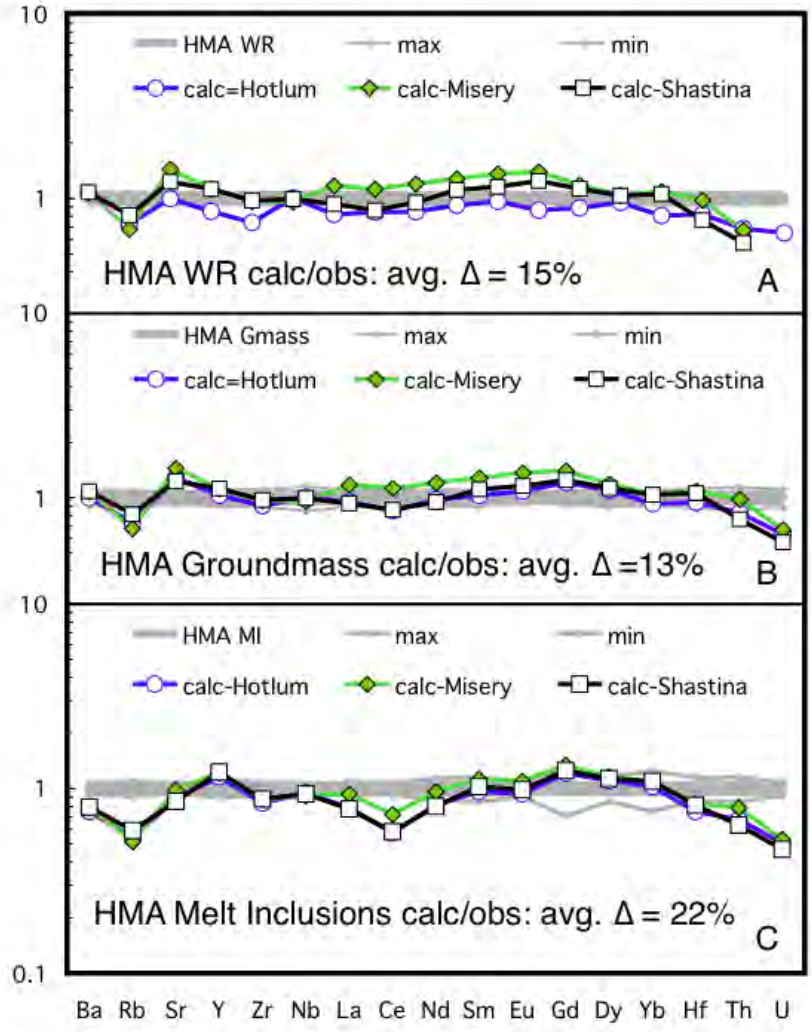
10
1
0.1
HMA WR
max
min
calc=Hotlum
calc-Misery
calc-Shastina
HMA WR calc/obs: avg. Δ = 15%
A
HMA Gmass
HMA Groundmass calc/obs: avg. Δ =13%
B
HMA MI
HMA Melt Inclusions calc/obs: avg. Δ = 22%
C
Ba Rb Sr Y Zr Nb La Ce Nd Sm Eu Gd Dy Yb Hf Th U

Table 1. Compositions of HMA whole rock samples from Whaleback quarry

Sample No.	MS-HMA2	MS-11-04	MS-HMA8	MS-12-04	MS-16-04	MS-HMA11
Sample type	ejecta block	ejecta block	ejecta block	ejecta block	ejecta block	ejecta block
Sequence #	1	1'	2	3	4	5
XRF major elements (wt.%), normalized to 100% sum						
SiO_2	58.44	-	57.81	58.29	58.30	57.86
TiO_2	0.593	-	0.598	0.585	0.585	0.584
Al_2O_3	15.24	-	14.77	14.77	14.73	14.55
FeO*	5.52	-	5.81	5.59	5.58	5.70
MnO	0.103	-	0.107	0.104	0.104	0.106
MgO	7.93	-	8.63	8.42	8.46	9.10
CaO	8.00	-	8.33	8.16	8.19	8.23
Na_2O	3.26	-	3.08	3.18	3.17	3.05
K_2O	0.78	-	0.72	0.77	0.76	0.69
P_2O_5	0.132	-	0.134	0.130	0.130	0.126
XRF trace elements (ppm)						
Ni	105	-	111	119	119	126
Cr	489	-	527	540	550	592
Sc	23	-	25	25	25	24
V	157	-	162	162	160	156
Ba	193	-	179	187	187	170
Rb	16	-	14	14.5	14.3	13
Sr	728	-	774	756	753	749
Zr	88	-	88	86	86	82
Y	11.0	-	11.0	11.4	11.3	11.0
Nb	2.4	-	2.3	3.6	3.7	1.9
Ga	16	-	17	18	17	15
Cu	35	-	39	57	52	47
Zn	61	-	60	56	55	56
La	15	-	12	10	10	12
Ce	22	-	24	27	23	24
Sr/Y	66.2	-	70.4	66.3	66.6	68.1
Mg# (X-fe3=0.1)	74.0	-	74.6	74.9	75.0	76.0

ICP-MS (ppm)	MS-HMA2	MS-11-04	MS-HMA8	MS-12-04	MS-16-04	MS-HMA11
Sc	21.8	22.2	23.2	22.6	22.9	22.6
V	-	154	-	160	157	-
Co	-	31.3	-	32.0	32.0	-
Ni	-	119	-	120	122	-
Cu	-	57	-	57	58	-
Zn	-	55	-	53	65	-
Ga	-	18.2	-	17.6	17.5	-
B [a]	-	*8.4* [c]	-	6.6	6.6	-
Li	-	11.30	-	10.95	10.95	-
Be	-	0.91	-	0.90	0.90	-
Cs	0.87	0.94	0.79	0.90	0.90	0.73
Rb	15.2	15.5	13.7	13.7	14.6	12.8
Sr	724	774	783	775	765	754
Y	11.05	13.00	10.95	12.10	12.35	10.53
Zr	87	102	87	97	96	82
Nb	2.50	2.75	2.37	2.55	2.50	2.25
Ba	195	195	179	194	190	173
La	10.56	11.00	10.97	10.60	10.40	10.18
Ce	23.46	22.00	24.61	22.35	22.35	22.51
Pr	3.12	3.13	3.28	3.00	2.93	3.03
Nd	12.64	13.40	13.33	12.45	12.25	12.32
Sm	2.71	2.76	2.74	2.50	2.50	2.60
Eu	0.84	0.90	0.87	0.80	0.82	0.83
Gd	2.42	2.81	2.48	2.55	2.59	2.32
Tb	0.38	0.42	0.37	0.40	0.39	0.36
Dy	2.18	2.28	2.12	2.10	2.10	2.07
Ho	0.44	0.43	0.44	0.40	0.39	0.41
Er	1.18	1.20	1.17	1.10	1.10	1.08
Tm	0.168	0.180	0.168	0.200	0.182	0.157
Yb	1.05	1.13	1.03	1.00	1.02	1.00
Lu	0.167	0.170	0.163	0.200	0.177	0.157
Hf	2.45	2.40	2.46	2.25	2.23	2.29
Ta	0.185	0.180	0.169	0.200	0.183	0.163
Pb	3.94	4.05	3.64	3.80	3.98	3.48
Th	2.09	2.04	2.00	1.90	1.90	1.89
U	0.75	0.710	0.69	0.700	0.693	0.64
Tl	-	0.075	-	0.100	0.091	-

Sr/Y	65.5	59.5	71.5	64.0	61.9	71.6
$^{87}Sr/^{86}Sr$	-	0.702990	-	0.703059	0.703055	-
$^{143}Nd/^{144}Nd$	-	-	-	-	-	-
$^{206}Pb/^{204}Pb$	-	18.898	-	18.865	18.863	-
$^{207}Pb/^{204}Pb$	-	15.596	-	15.581	15.582	-
$^{208}Pb/^{204}Pb$	-	38.498	-	38.451	38.448	-

XRF major and trace element analyses were done at WSU Geoanalytical Laboratories
ICP-MS analyses on MS-xx-04 samples were done at Rice University; analysts: A. Agra
Sr and Pb isotopic analyses were done at University of Arizona; analyst: J. Chesley
Data for sample 85-41b are from [1] Rice U. (this study), [2] Grove et al. (2002), and [3] M
[a] B determined by ICP-AES at Rice University; analysts: W.P. Leeman, A. Agranier
[b] Numbers in brackets for Co and Ta in sample 85-41b are anomalously high due to WC
[c] Data in italics are excluded from element statistics (one outlier each for B and Cs)
Dash indicates no analysis was done

(S-17 location)

MS-HMA14 ejecta block 6	MS-18-04 dike chilled margin 7a	MS-HMA15 dike 7b	Average	SD	RSD	85-41b Rice Univ.
						Rice
58.12	-	58.05	58.14	0.255	0.4%	-
0.585	-	0.580	0.59	0.006	1.0%	-
14.67	-	14.59	14.79	0.236	1.6%	-
5.70	-	5.74	5.65	0.106	1.9%	-
0.105	-	0.107	0.105	0.001	1.4%	-
8.83	-	8.93	8.56	0.399	4.7%	-
8.17	-	8.13	8.18	0.108	1.3%	-
2.98	-	3.05	3.12	0.102	3.3%	-
0.72	-	0.69	0.74	0.035	4.7%	-
0.128	-	0.122	0.13	0.003	2.2%	-
122	-	128	117	8	6.6%	-
593	-	603	548	40	7.3%	-
24	-	24	24	1	3.1%	-
160	-	151	159	2	1.5%	-
177	-	177	182	8	4.6%	-
14	-	13	14.3	1.0	6.9%	-
763	-	760	754	15	2.0%	-
85	-	86	86	2	2.6%	-
10.0	-	12.0	11.0	0.5	4.5%	-
2.0	-	2.2	2.7	0.8	30.1%	-
16	-	16	16.4	1.0	5.9%	-
20	-	37	42	13	32.0%	-
58	-	59	58	2	4.3%	-
14	-	9	12.0	2.2	18.4%	-
20	-	23	23.3	2.2	9.5%	-
76.3	-	63.3	69.0	3.9	5.7%	-
75.4	-	75.5	75.0	0.68	0.9%	-

MS-HMA14	MS-18-04		Average	SD	RSD	85-41b
22.8	22.8	23.1	22.7	0.4	1.9%	24.6
-	158		157.1	2.5	1.6%	172
-	34.3		32.4	1.3	4.1%	*[64.9]* [b]
-	143		125.8	11.6	9.2%	134
-	65		59.4	4.0	6.7%	58
-	57		57.5	5.1	8.8%	50
-	17.7		17.7	0.3	1.8%	16.4
-	6.3		6.5	0.2	2.7%	6.4
-	11.90		11.3	0.4	4.0%	11.26
-	0.87		0.89	0.02	1.9%	0.79
0.79	0.97	*0.48* [c]	0.86	0.08	9.7%	0.779
13.3	16.1	11.9	14.1	1.4	9.6%	13.8
763	794	753	765.0	20.3	2.6%	776
10.57	12.80	10.71	11.6	1.0	8.6%	12.24
84	104	84	91.5	8.3	9.1%	99.4
2.32	2.82	2.30	2.48	0.20	8.0%	3.29
179	205	177	187.3	10.9	5.8%	191
10.31	11.10	10.29	10.6	0.3	3.2%	11.1
22.97	22.50	22.71	22.8	0.8	3.5%	23.7
3.03	3.17	3.06	3.08	0.10	3.3%	3.13
12.40	13.60	12.62	12.8	0.5	4.1%	13.0
2.56	2.75	2.67	2.64	0.11	4.0%	2.60
0.82	0.90	0.86	0.85	0.04	4.2%	0.91
2.35	2.78	2.37	2.52	0.18	7.1%	2.83
0.35	0.42	0.36	0.38	0.02	6.5%	0.41
2.10	2.26	2.12	2.15	0.08	3.6%	2.19
0.42	0.42	0.42	0.42	0.02	4.0%	0.40
1.11	1.19	1.14	1.14	0.04	3.9%	1.15
0.161	0.179	0.163	0.173	0.013	7.8%	0.17
1.01	1.13	1.04	1.04	0.05	4.9%	1.04
0.154	0.169	0.159	0.168	0.014	8.2%	0.15
2.33	2.44	2.36	2.36	0.09	3.7%	2.38
0.165	0.178	0.169	0.177	0.012	6.6%	*[1.92]* [b]
3.60	4.44	3.51	3.83	0.31	8.1%	-
1.93	2.11	1.94	1.98	0.08	4.3%	2.05
0.68	0.739	0.65	0.69	0.04	5.2%	0.713
-	0.053	-	0.08	0.02	25.9%	-

72.2	62.0	59.5	65.3	5.2	7.9%	63.4
-	0.702932	-	0.703009	0.000060	0.009%	-
-	-	-	-	-	-	-
-	18.865	-	18.873	0.017	0.089%	-
-	15.586	-	15.586	0.007	0.044%	-
-	38.453	-	38.463	0.024	0.062%	-

nier, W.P. Leeman, C.-T. Lee; MS-HMA samples were analyzed at WSU Geoanalytical

Magna et al. (2006)

contamination; these are ignored

85-41b	85-41b
Grove et al. (2002)	**Magna et al. (2006)**
G2002	M2006
57.86	-
0.60	-
14.67	-
5.69	-
0.11	-
8.88	-
8.13	-
3.18	-
0.72	-
0.16	-
131	-
495	-
25	-
185	-
189	-
17.0	-
812	-
92	-
12	-
3.6	-
-	-
56	-
56	-
-	-
-	-
67.7	-
75.6	-

85-41b	85-41b
25.0	19.0
185	-
[62]	-
131	128
56	-
56	-
-	-
-	-
-	10.20
-	-
1.100	0.590
17.0	12.3
812	741
12.0	10.1
92.0	83.0
3.60	3.50
189	167
10.7	10.3
24.2	23.1
3.33	3.06
12.9	12.3
2.60	2.70
0.85	0.92
2.42	2.30
0.35	0.34
1.94	1.88
0.40	0.39
1.07	1.14
0.16	0.16
1.05	1.05
0.16	0.16
3.45	2.70
-	-
-	3.5
1.69	1.90
0.680	0.610
-	-

67.7	73.4
0.702993	-
0.512974	-
18.851	-
15.567	-
38.405	-

Lboratories

Table 2. HMA Groundmass, whole-rock, and melt inclusion compositions

This paper	Groundmass Average [a] (n = 7)	s.d.	HMA WR Average [b] (n = 7/9)	s.d.	HMA MI Average [c] (n = 5)	s.d.	PBA MI Average [c] (n = 14)	s.d.
SiO_2	61.63	1.20	58.14	0.25	58.48	1.17	55.62	1.43
TiO_2	0.68	0.09	0.59	0.01	0.70	0.03	0.68	0.03
Al_2O_3	16.28	1.40	14.79	0.24	16.86	1.12	15.08	0.73
	0.00		0.00		0.00		0.00	
FeO*	4.49	0.33	5.65	0.11	5.68	0.39	4.37	0.33
MnO	0.08	0.01	0.10	0.001	0.10	0.01	0.09	0.01
MgO	3.60	0.50	8.56	0.40	5.45	0.39	8.88	0.99
CaO	7.99	0.60	8.18	0.11	8.74	0.60	12.35	0.96
Na_2O	4.10	0.30	3.12	0.10	2.86	0.56	2.25	0.43
K_2O	1.00	0.15	0.74	0.03	0.92	0.11	0.37	0.07
P_2O_5	0.15	0.02	0.130	0.003	0.21	0.08	0.32	0.07
Mg# [g]	64.6	-	76.1	-	66.8	-	81.0	-
Fo [g]	87.0	-	91.5	-	87.7	-	93.5	-
Trace elements [h]								
U	0.96	0.11	0.69	0.04	0.92	0.08	0.37	0.08
Rb	19.5	1.9	14.1	1.4	20.5	2.0	4.8	2.1
Pb	5.2	0.6	3.83	0.31	6.4	0.8	3.1	0.7
Nb	3.16	0.47	2.48	0.20	3.10	0.07	1.5	0.2
Ce	28.6	3.1	22.8	0.8	33.3	2.2	28.2	3.6
Ba	221	21	187	11	256	16	80	18
La	12.1	1.3	10.6	0.3	11.4	1.0	9.8	0.5
Ta	0.20	0.01	0.18	0.01	0.18	0.05	0.08	0.02
Th	2.2	0.3	1.98	0.08	2.0	0.3	1.04	0.21
Pr	3.4	0.2	3.08	0.10	3.6	0.3	3.3	0.3
Zr	101	11	91.5	8.3	95	8	68	7
Nd	14.1	1.4	12.8	0.5	13.8	1.9	12.6	0.9
Sm	2.8	0.3	2.64	0.11	2.7	0.4	2.3	0.5
Eu	0.90	0.04	0.85	0.04	0.96	0.09	0.8	0.1
Yb	1.1	0.1	1.04	0.05	1.2	0.3	0.8	0.2
Sr	801	61	765	20	867	54	1047	73
Hf	2.4	0.3	2.36	0.09	2.8	0.4	1.8	0.3
Er	1.1	0.1	1.14	0.04	1.0	0.3	0.9	0.3
Y	10.5	1.1	11.6	1.0	11.1	1.1	7.9	1.3

Dy	1.9	0.2	2.15	0.08	2.0	0.3	1.4	0.2
Gd	2.2	0.2	2.52	0.18	2.1	0.6	1.7	0.5
Sc	15.4	2.0	22.7	0.4	28	7	31	6
Cr	59	22	548	40	361	246	1019	1395

Notes:

˘ Groundmass is from sample MS-04-16 (this study); analyses by EMP (major elements) an

˜ Average HMA whole-rock (from Table 1, this study); based on 7 major element and 9 trace

ˇ Compositions of olivine-hosted HMA- and PBA-type melt inclusions are from Ruscitto et al

˘ Enrichment Factor = Groundmass concentration/Average WR concentration.

ˇ Mg# and equilibrium olivine Fo are calculated assuming Xfe3 = 0.2.

f Melt inclusions in Type 1 antecrystic low Mg# (71-73) cores

g For all analyses except 1st column, calculated Mg# and olivine Fo content assume X-fe3 =

h Trace element data are not corrected for olivine addition.

Enrichment Factor [d]	Opx [f] (71-73) MI Average (n = 5)	s.d.	Ruscitto et al. (2011)	HMA MI Average [c] (n = 5)	PBA MI Average [c] (n = 14)
1.06	67.75	1.70		58.46	53.54
1.15	1.10	0.30		0.70	0.58
1.10	17.14	0.90		16.82	12.93
				0.00	0.00
0.80	3.76	0.05		5.70	7.02
0.76	0.07	0.05		0.10	0.07
0.42	0.59	0.37		5.54	12.92
0.98	4.41	0.73		8.70	10.56
1.31	3.21	0.37		2.86	1.79
1.35	1.68	0.06		0.91	0.31
1.15	0.29	0.08		0.22	0.27
-	24.8	-		67.1	79.4
-	56.0	-		87.8	92.4
1.39				0.92	0.37
1.38				20.5	4.8
1.36				6.4	3.1
1.27				3.10	1.5
1.25				33.3	28.2
1.18				256	80
1.14				11.4	9.8
1.11				0.18	0.08
1.11				2.0	1.04
1.10				3.6	3.3
1.10				95	68
1.10				13.8	12.6
1.06				2.7	2.3
1.06				0.96	0.8
1.06				1.2	0.8
1.05				867	1047
1.02				2.8	1.8
0.96				1.0	0.9
0.91				11.1	7.9

0.88	2.0	1.4
0.87	2.1	1.7
0.68	28	31
0.11	361	1019

d LA-ICPMS (trace elements); X-fe3 = 0.22.
e element analyses.
. (2011); cf. Supplement B.

= 0.15.

Table 3. Least-squares mixing models for HMA based on major elements

Model	Dacite variant	Component proportions: Dacite	BA 85-44	Trinity UM	Cpx2 Mg#85	Fo87	An60	$\Sigma(Res)^2$
Type: HMA whole-rock average								
	Avg. all	0.569	0.306	0.051	0.083	-0.006	-	0.240
	Hotlum	0.583	0.277	0.050	0.091	-	-	0.166
	Shastina	0.563	0.311	0.048	0.077	-	-	0.191
	Misery	0.554	0.306	0.050	0.091	-	-	0.229
	Sargents	0.622	0.234	0.054	0.097	-	-	0.370
			HAOT 85-38					
	Avg. all	0.636	0.230	0.042	0.096	-	-	0.311
Type: HMA low-Ca melt inclusions (HMA type)								
	Avg. all	0.515	0.507	-	0.041	-0.052	-0.006	0.467
	Hotlum	0.526	0.500	-	0.046	-0.051	-0.016	0.460
	Shastina	0.507	0.543	-	0.031	-0.055	-0.023	0.415
	Misery	0.499	0.541	-	0.043	-0.055	-0.025	0.463
	Sargents	0.563	0.442	-	0.054	-0.045	-0.006	0.573
Type: HMA groundmass								
	Avg. all	0.821	0.137	-	0.080	-0.045	0.008	0.379
	Hotlum	0.838	0.126	-	0.087	-0.044	-0.008	0.295
	Shastina	0.806	0.196	-	0.063	-0.050	-0.020	0.385
	Misery	0.794	0.191	-	0.083	-0.049	-0.022	0.296
	Sargents	0.898	0.030	-	0.100	-0.033	0.009	0.456